Cold Atom Ring Laser

by

Balázs Megyeri

A thesis submitted to
the University of Birmingham
for the degree of
DOCTOR OF PHILOSOPHY

Ultracold Atoms Group
School of Physics and Astronomy
University of Birmingham

September 2018

Abstract

This thesis will describe a cold atom ring laser that uses a cloud of magneto-optically trapped potassium atoms as a gain medium and a ring cavity for feedback. Some upgrades to the experiment were necessary, which include a new imaging axis in the vacuum system, a new atom source, alignment of some new optics and detectors to measure the powers and transverse intensity profiles of both counterpropagating cavity modes, and a new tapered amplifier for the magneto-optical trapping beams. The lasing threshold, gain mechanism, intensity correlations, and lasing into the two counterpropagating cavity modes were investigated. The results showed several transverse patterns at the lasing outputs, a threshold as a function of atom number, Mollow gain, a flat second-order coherence above threshold, clearly distinguishable from that of fluorescence, nonreciprocity of the TEM_{00} transverse mode as a function of cavity length, and anticorrelated counterpropagating modes.

Acknowledgements

I would like to thank my supervisor Jonathan Goldwin for the opportunity to work on this exciting project, the Defence Science and Technology Laboratory for funding us, and Graeme for being helpful and hard-working in our lab even when everything seemed to break down. I hope the experiment will continue to work for a long time and wish you great success with the new measurements. I received great support from the rest of the Ultracold Atom Group as well, mostly including Rob and Andreas who have recently left the project. I would also like to thank Vincent, Giovanni, Mike, Plamen, Chris, Ania, and Kai for all the advice they have given over the years, and loan of equipment.

Contents

Abstract **iii**

Acknowledgements **v**

1 Introduction **1**

1.1 Ring Laser Gyroscope, Active Clock, and Group Index 1

1.2 Lasers 2

1.3 Mollow Gain 2

1.4 Lasing with Cold Atoms 3

1.5 Lasing with Cold Atoms in a Ring Cavity 3

1.6 Thesis Outline 4

1.7 Publications Arising from This Work 4

2 Theoretical Background **7**

2.1 Absorption and Dispersion 7

2.1.1 Electric Susceptibility 7

2.1.2 Phase and Group Velocities 8

2.1.3 Absorption and Gain Resonances 9

2.2 Mollow gain in Two-Level Atoms 11

2.3 Optical Cavity 13

2.3.1 Empty Ring Cavity 14

2.3.2 Effect of Medium 18

3 Magneto-Optically Trapped ^{39}K Atoms 25

3.1 Vacuum System 25

3.1.1 Upgrades to the Old System 27

3.1.2 New Atom Source 28

3.1.3 Baking the New Vacuum System 31

3.1.4 Ion Pump 32

3.2 Laser System 33

3.2.1 D_2 Hyperfine Structure of ^{39}K 33

3.2.2 Overview of Laser System 34

3.2.3 New Tapered Amplifier Design 35

3.3 Coils and Magnetic Field 39

3.4 Measurements 42

4 Magneto-Optically Trapped ^{39}K Atoms in a Ring Cavity 45

4.1 Ring Cavity 45

4.1.1 Dimensions and Parameters 46

4.1.2 Laser System 48

4.2 Alignment and Strong Coupling 51

4.2.1 Optimisation of the MOT Position 51

4.2.2 Rabi Splitting 53

5 Bidirectional Ring Laser 57

5.1 Mollow Gain in ^{39}K Atoms 57

5.1.1 Gain Measurement 58

5.1.2 Determining the Gain Mechanism 62

5.2 Transverse Patterns of Laser Outputs 64

5.2.1 Theory of Hermite-Gaussian Modes 64

5.2.2 Tranverse Patterns of Lasing Modes 65
5.3 Onset of Lasing and Second-Order Coherence $g^{(2)}$ 69
5.3.1 Threshold Measurement 69
5.3.2 Theory of Second-Order Coherence 70
5.3.3 $g^{(2)}$ Measurement 73
5.4 Counterpropagating Lasing Modes and Nonreciprocity 76
5.4.1 CW and CCW Spectra 76
5.4.2 Cross-correlation 79
5.5 Conclusion on Bidirectional Lasing 81

6 Outlook **83**
6.1 Raman Gain and Four-Wave Mixing 84
6.2 Active Clock 86
6.3 Gyroscope 87

Appendices

A Stimulated Brillouin Scattering **89**
A.1 Theory of Stimulated Brillouin Scattering 89
A.2 Experimental Setup 90
A.3 Threshold 92
A.4 Pulse Advancement 93

List of Figures **95**

List of Tables **103**

List of References **105**

Chapter 1

Introduction

1.1 Ring Laser Gyroscope, Active Clock, and Group Index

Unlike standing-wave linear cavities, ring cavities can have two counter-propagating travelling-wave modes. If a gain medium is introduced, the configuration is called a ring laser. It can be unidirectional (missing one of the two travelling waves) or bidirectional.

One of the main applications of bidirectional ring lasers is rotation measurement. In general, laser sensors write physical observables onto the output of a laser. In the application of bidirectional ring lasers, the frequencies of the two outputs give the key information. Bidirectional ring lasers exploit the Sagnac effect, which is the splitting of the counterpropagating resonance frequencies, due to different phase shifts caused by rotation [1–4]. The frequency detuning between the two counterpropagating cavity modes is inversely proportional to the group index, which is related to the slope of the refractive index of the gain medium. This slope is taken around the

non-rotating cavity resonance frequency. It can make the system sensitive (negative slope) or insensitive (large and positive slope) to rotation of the cavity mirrors. A single gain peak that is necessary in lasers gives normal dispersion and a positive slope (group index), but there are ways to turn that positive slope into a negative one, for example, by introducing two nearby gain peaks (there is more detail on this in Section 6.3).

In conventional lasers the cavity resonances are narrower than the gain resonances and the cavity selects the output frequency. In order to build a frequency standard, the output frequency should depend on a stable atomic reference and not on the environment (cavity length and movement of the cavity mirrors), which is called an active clock and is also achievable with dispersion.

1.2 Lasers

A ring laser gyroscope also has to satisfy the requirements of a laser, which usually include a pumping mechanism (a source of energy) and a feedback mechanism. The pumping mechanism creates population inversion (typically involving multiple energy levels) that is necessary in order for stimulated emission to outcompete absorption. The feedback mechanism ensures that stimulated emission suppresses spontaneous emission.

1.3 Mollow Gain

In this work, Mollow gain was used. Unlike most lasing schemes, it does not require 3 or 4 levels, separate pump mechanisms, and population inversion in the traditional sense, that is, in the eigenstates of the non-interacting atom. It does however need a strong pump field that splits the 2 eigenstates into

4 levels in the coupled atom-light system. Absorption of two pump photons is followed by emission of two photons at the Mollow sideband frequencies (see Section 2.2).

1.4 Lasing with Cold Atoms

The first cold atom laser was demonstrated using cesium and its hyperfine structure that is accessible at low temperatures also provides a rich variety of dispersive features [5–9]. Laser cooled atoms have been popular frequency standards. More recent work on active clocks suggests the accuracy of frequency standards can further be improved by dispersion and lasing [10–15]. Narrow-linewidth transitions that depend on magnetic field can be used as magnetometers [16].

Since the cesium cold atom laser, some other laser cooled atomic species have also successfully been used as a gain medium, for example, rubidium [17–19], and ytterbium [20]. Mirrorless lasing (or random lasing) with cold atoms has been demonstrated [21–23], where the atomic density, atomic motion, and scattering from atoms work as a feedback mechanism.

1.5 Lasing with Cold Atoms in a Ring Cavity

As explained at the beginning of this chapter, a gyroscope needs two travelling-wave modes. In order to achieve this, the easiest choice is to use three mirrors in a triangular ring cavity. Other works on cold atom lasers that have been published so far only dealt with linear cavities.

Due to lack of Doppler broadening at low temperature, narrow dispersive features are feasible with cold atoms. As the Sagnac effect scales with the area of the interferometer, the size of the device will limit its sensitivity

and that does not give much freedom as sensors should be as compact as possible. However, dispersion control could also enhance the sensitivity and the first step is to create a cold atom ring laser that will offer dispersion control in the future.

1.6 Thesis Outline

Chapter 2 will summarise how a cold atom ring laser works and the possible applications. Chapter 3 and 4 will briefly explain the recent upgrades to the magneto-optical trapping design and the ring cavity. Chapter 5 will focus on the main results, that is, the lasing threshold, gain mechanism, intensity correlations, and lasing into the two counterpropagating cavity modes. Chapter 6 will come back to the applications and lay out the next steps in the experiment. This thesis will aim at recent achievements and whenever something is not explained in detail, earlier theses [24–27] should be referred to.

1.7 Publications Arising from This Work

- B. Megyeri, G. Harvie, A. Lampis, and J. Goldwin. Directional Bistability and Nonreciprocal Lasing with Cold Atoms in a Ring Cavity. Physical Review Letters **121** (16), 163603 (2018).

  Main contributions: refurbishment of the experiment, new measurement setups and alignment, data acquisition and analysis for the threshold curve, second-order coherence, and cross-correlation.

- B. Megyeri, A. Lampis, G. Harvie, R. Culver, and J. Goldwin. Why material slow light does not improve cavity-enhanced atom detection. Journal of Modern Optics, **65** (5-6), 723-729 (2017).

Main contributions: numerical simulations and data analysis.

- R. Culver, A. Lampis, B. Megyeri, K. Pahwa, L. Mudarikwa, M. Holynski, Ph. W. Courteille, and J. Goldwin. Collective strong coupling of cold potassium atoms in a ring cavity. New Journal of Physics, **18** (11), 113043 (2016).

  Main contributions: assembling and baking the vacuum system, the new 2D MOT chamber, new 3D MOT coils, and servo-loop electronics.

- A. Lampis, R. Culver, B. Megyeri, and J. Goldwin. Coherent control of group index and magneto-optical anisotropy in a multilevel atomic vapor. Optics Express **24** (14), 15494-15505 (2016).

  Main contributions: theoretical models, simulations, and data analysis.

Chapter 2

Theoretical Background

2.1 Absorption and Dispersion

This section will explain the relation between gain, absorption, normal and anomalous dispersion.

2.1.1 Electric Susceptibility

When propagation of the electric field through a medium is described, the slowly varying amplitude approximation is commonly used. It roughly means that the electric field does not change much over a wavelength. The medium with susceptibility $\chi(\omega)$ (taken at frequency ω) causes the electric field $\vec{E}(z,\omega)$ with a wave vector k (taken along one dimension) to change between spatial points 0 and z_0 accordingly to

$$\vec{E}(z_0,\omega) = \vec{E}(0,\omega)e^{ikz_0\frac{1}{2}\,\mathrm{Re}(\chi(\omega))}e^{-kz_0\frac{1}{2}\,\mathrm{Im}(\chi(\omega)}, \tag{2.1}$$

describing an exponential decay of the amplitude when $0 < \mathrm{Im}(\chi(\omega))$, which, for this reason, can be thought of as the absorption coefficient. This is

derived in [28] and the same convention on factors of 2 will be used in this thesis. There is absorption when $\mathrm{Im}(\chi(\omega)) > 0$, and there is gain when $\mathrm{Im}(\chi(\omega)) < 0$. Note that Equation (2.1) also quantifies the extra phase shift $kz_0\frac{1}{2}\,\mathrm{Re}(\chi(\omega))$ caused by the medium.

The above approximation is also called the slowly varying envelope approximation or (although usually in a slightly different context) paraxial approximation. There is not a unique convention on the exact form and some derivations also involve extra factors of 2, -1, or i in the definition of χ (and therefore also in Equation (2.1)), depending on what is more convenient in applications. Another treatment (aiming at conventional lasers) with similar results, called plane-wave approximation, can be found in [29].

It is also important to note that, as a consequence of causality, the real and imaginary parts of the susceptibility are not independent, thus either one determines the other through the Kramers-Kronig relations [30].

2.1.2 Phase and Group Velocities

In the case of a plane wave that has a certain frequency ω and a wave vector $\vec{k}$ ($|\vec{k}| = k$), the velocity of propagation (i.e. the phase velocity) is

$$v = \frac{\omega}{k} = \frac{c}{n(\omega)}, \tag{2.2}$$

where c is the speed of light in vacuum and $n(\omega) := \sqrt{1+\chi(\omega)}$ is the refractive index. When $n \simeq 1$,

$$\mathrm{Re}(n) \simeq \sqrt{1+\mathrm{Re}(\chi)} \simeq 1 + \frac{1}{2}\,\mathrm{Re}(\chi). \tag{2.3}$$

In laser sensors the light beam consists of many modes and it is much more important what happens to the shape of the beam or pulse, which is char-

acterised by the group velocity

$$v_g = \frac{d\omega}{dk}. \tag{2.4}$$

It can also be thought of as the slope of the first-order term in $\omega(k)$. Analogously to the refractive index (or phase index)

$$n(\omega) = \frac{c}{v},$$

the group index is defined by

$$n_g = \frac{c}{v_g}.$$

Using (2.2) and (2.4), it can be written in the form

$$n_g = n(\omega) + \omega \frac{dn(\omega)}{d\omega}. \tag{2.5}$$

When $v_g < v$ ($n_g > n$), it is called slow light and requires a large group index, whereas $v_g > v$ ($n_g < n$) means fast light and requires a small group index [29–32]. An example of how n_g can be measured is shown in Appendix A. n_g is a parameter that could enhance the Sagnac effect in ring laser gyroscopes as explained in Chapter 1.

2.1.3 Absorption and Gain Resonances

The purpose of this section is to show that a Lorentzian absorption peak generally results in fast light, whereas a gain peak gives slow light. Even though potassium has more than two energy levels, many measurements can be well approximated by only two levels. Therefore, these examples will

focus on only two levels. Using a Lorentzian susceptibility

$$\chi(\Delta) \propto -\frac{\Omega}{2}\frac{1}{\Delta - i\Gamma/2}, \tag{2.6}$$

where Δ is the probe beam detuning from the centre of the peak and $\Omega = -\frac{\langle \hat{E}\hat{\mu} \rangle}{\hbar}$ is the Rabi frequency [29, 33] of the probe beam ($\hat{\mu} = -e\hat{r}$ is the dipole operator and $\hat{E}$ is the quantised electric field, which is not used explicitly in this thesis). Most absorption and gain peaks can be approximated by a Lorentzian. To make the calculation simpler, we can assume that only the sign of the peak is different when we change the formula in order to turn absorption into gain.

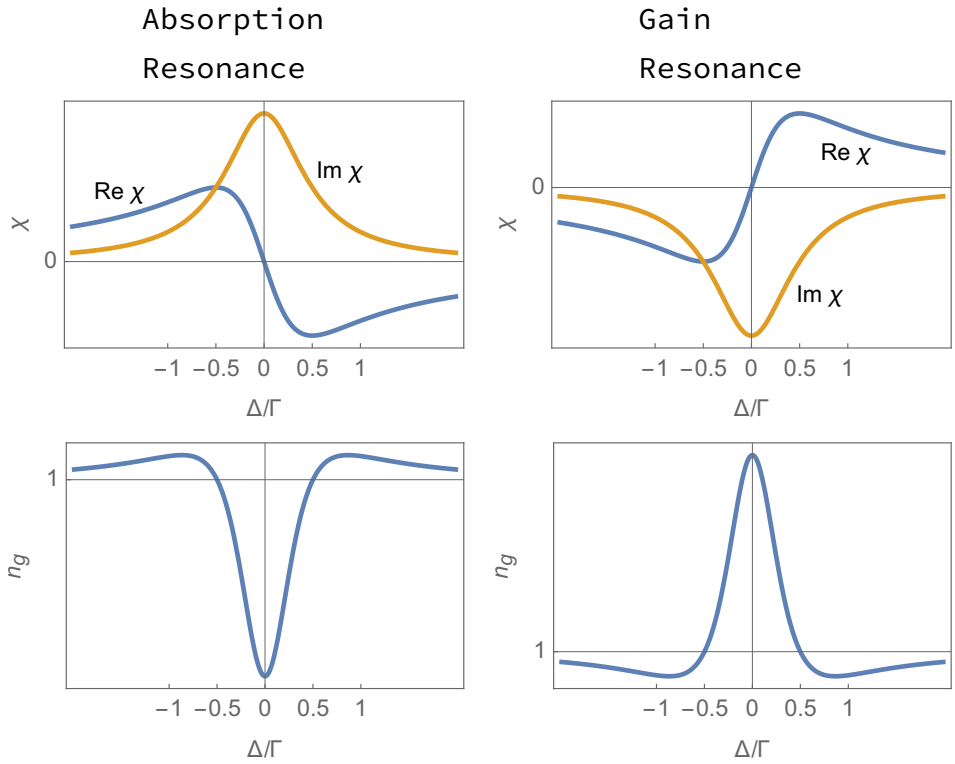

Figure 2.1 Slow light and fast light during absorption and gain. The susceptibility and the group index are shown against the detuning. Similar curves can be found in [34].

It is well-known that a single absorption peak can be given by a two-level atom and a probe beam swept across resonance. While this configuration might look oversimplified and too theoretical, with a feedback mechanism it can also be a laser [35–38] and is actually used in the experiment. The main difference is that there has to be a strong pump beam in order for a probe beam at a different frequency (or the lasing mode when it works as a laser above threshold) to be amplified. This mechanism is called Mollow gain and is a consequence of the interaction between the pump beam and the two-level atom, which splits the free energy levels into the dressed states that allow for population inversion (see Section 2.2).

2.2 Mollow gain in Two-Level Atoms

When a two-level system is driven by a strong pump field, the eigenstates of the coupled atom-light system will be different to those of the non-interacting atom, and some transitions can also provide gain [35–37, 39–42]. The full calculation is lengthy, but this section will illustrate the underlying physics in order to understand the results presented in Chapter 4.

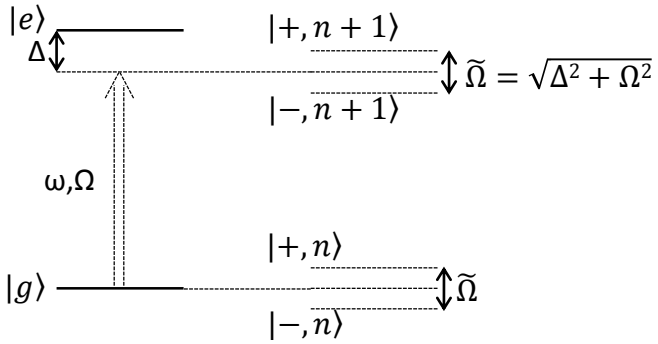

Figure 2.2 Dressed states of the coupled atom-light system. $|g\rangle$ and $|e\rangle$: ground and excited states of the non-interacting two-level atom, ω: the pump laser frequency, Ω: pump laser Rabi frequency, $|+, n\rangle$ and $|-, n\rangle$: eigenstates of the atom-light system with n photons, and $\tilde{\Omega}$: generalised Rabi frequency.

Ω is the Rabi frequency describing the strength of the pump field. When $\Omega = 0$, the free eigenstates $|g\rangle$ and $|e\rangle$ apply. As Ω is increased, the atomic levels split symmetrically into $|+, n\rangle$ and $|-, n\rangle$. The splitting between $|+, n\rangle$ and $|-, n\rangle$ is the generalised Rabi frequency $\tilde{\Omega}$.

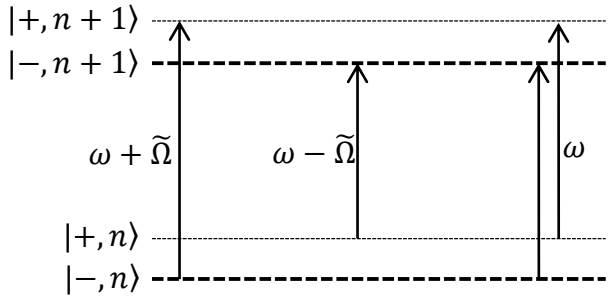

Figure 2.3 The transitions between the dressed states. The thicker dashed lines indicate that the population is larger in the $|-, \cdot\rangle$ states.

There are three resonance frequencies in this system: $\omega - \tilde{\Omega}$, ω, and $\omega + \tilde{\Omega}$ (Figure 2.3). It is important to emphasise that the centre feature always occurs at the pump laser frequency, which can be different to the two-level resonance frequency. When $\Delta = 0$, which means that ω is on resonance with the $|g\rangle \rightarrow |e\rangle$ transition, the energy levels split symmetrically around the bare states $|g\rangle$ and $|e\rangle$. This is called the Mollow triplet. It is usually only explained when $\Delta = 0$, but in this thesis the pump laser will be red detuned from the relevant transition, since it also serves as a cooling beam.

In the four-level system that consists of the dressed states illustrated above, population inversion is possible and gain is observed when the system is probed at the frequency

$$\omega_{\text{probe}} = \omega - \sqrt{\Delta^2 + \Omega^2} \tag{2.7}$$

in the presence of the pump beam. The full absorption coefficient that also

describes the peak heights (and therefore the amount of gain) is

$$\alpha = \frac{\Gamma}{2}\frac{|z|^2}{|z|^2+\Omega^2/2}\,\mathrm{Re}\left[\frac{(\Gamma+i\delta)(z+i\delta)-i\Omega^2\delta/(2z)}{(\Gamma+i\delta)(z+i\delta)(z^*+i\delta)+\Omega^2(\Gamma/2+i\delta)}\right] \tag{2.8}$$

as it appears in [17, 43]. $z = \Gamma/2 - i\Delta$, Γ is the natural linewidth of the $|g\rangle \to |e\rangle$ transition and $\delta = \omega_{\mathrm{probe}} - \omega$ is the probe detuning from the pump laser.

2.3 Optical Cavity

The main purpose of a cavity is to confine the optical field, enhancing the optical intensity and the interaction between the atom and the optical field. In lasers, cavities are most commonly used to provide feedback. Cavities also serve as interferometers in several applications [1–4, 44, 45]. This section will introduce the most important quantities that are used in this thesis. More detail can be found in [26, 29, 46].

The finite length and volume of cavities imply discrete frequencies of the confined field. These are called resonance frequencies. The resonance frequencies accumulate in resonance peaks with a certain width Δf_{FWHM} (full width at half maximum). The peaks are evenly spaced by the free spectral range

$$\mathrm{FSR} = \frac{c}{L}, \tag{2.9}$$

where c is the speed of light in vacuum and L is the round-trip length of the cavity. This assumes vacuum in the cavity. In general, the resonance frequencies are such that the round-trip phase shift, caused by dispersive media and propagation of light, has to be an integer multiple of 2π and the

difference between the nearest resonances is FSR. The cavity finesse is given by

$$\mathrm{F} = \frac{\mathrm{FSR}}{\Delta f_{\mathrm{FWHM}}}. \tag{2.10}$$

Analogously to the excited states of atoms, the finite frequency linewidth of cavity resonances corresponds to an exponential decay in the time domain, with the time constant of κ (energy decay time), where $\kappa = 2\pi\Delta f_{\mathrm{FWHM}}$ (i.e. FWHM linewidth in angular frequency). Therefore, in order to maintain the excitations of the cavity field, there has to be a driving (input) field either directly coupled to the cavity mode or scattered from the in-cavity medium into the cavity mode.

To model the interaction between the cavity field and the medium, it is important to know the cavity waist ($1/e^2$ radius of the transverse intensity profile) given by the cavity geometry. The experiment is aimed at TEM_{00} (i.e. a single Gaussian peak in the transverse intensity profile), but the waist is larger for higher-order transverse modes (see 5.2). A small waist in the medium is desirable so as to increase the intensity and interaction with the medium.

2.3.1 Empty Ring Cavity

Even without any dispersive media, transmission through a cavity already adds an extra phase shift to the free propagation, which implies changes to all quantities that depend on it. The effect of medium will then be included in the next section by a simple transformation. Let us consider the ring cavity geometry (Figure 2.4) that is also used in the experiment. There is more detail in [24, 26].

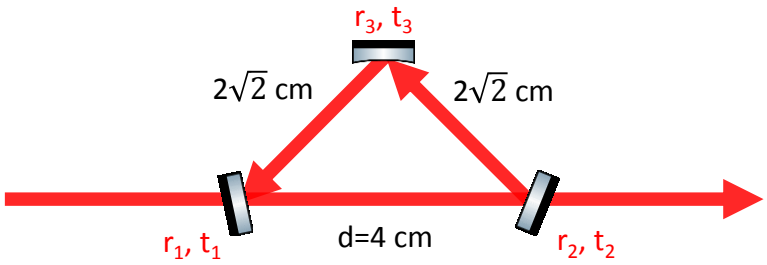

Figure 2.4 Ring cavity geometry and a probe beam (red). The distances between the mirrors are the same as in the experiment ($d = 4$ cm, $2\sqrt{2}$ cm, and $2\sqrt{2}$ cm along the probe beam). $r., t.$ denotes the amplitude reflection and transmission coefficients.

Some of the incident field is transmitted through the first two mirrors without hitting the third one, while the rest of it can perform an arbitrary number of round-trips and still contribute to transmission [24, 26, 29, 46]. Because of losses at the mirrors, each round-trip decreases the amplitude and intensity. The transmitted amplitude is the sum of the infinite series of slowly varying envelopes of the positive-frequency fields, $\sqrt{T} = t_1 t_2$, $\rho = r_1 r_2 r_3$ ($t.$ and $r.$ are the field transmission and reflection coefficients), L is the round-trip cavity length, d is the distance between the first two mirrors. Let us use the convention that the transmitted amplitude picks up an extra factor of complex i. In this convention the formulas do not depend on the direction of propagation through boundaries (with respect to high and low refractive indices) [29]. Therefore, transmission through two mirrors results in a factor of (-1). The transfer function (i.e. the transmitted amplitude

normalised to the incident amplitude) reads:

$$\begin{aligned} F(k) \quad = \quad & \left(-\sqrt{T}\right) e^{ikd} \\ & + \left(-\sqrt{T}\right) e^{ikd} \rho e^{ikL} \\ & + \left(-\sqrt{T}\right) e^{ikd} \rho^2 e^{i2kL} \\ & \vdots \\ & + \left(-\sqrt{T}\right) e^{ikd} \rho^n e^{inkL} \\ & \vdots \end{aligned} \tag{2.11}$$

This series can be summed up (there is more detail on the same cavity in [26]).

$$F(k) = -\sqrt{T} \frac{e^{ikd}}{1 - \rho e^{ikL}} \tag{2.12}$$

$$= -\sqrt{T} \frac{e^{ikd}\left(1 - \rho e^{-ikL}\right)}{(1-\rho)^2 + 4\rho \sin^2(kL/2)} \tag{2.13}$$

$$= -\sqrt{T} \frac{e^{ikd}\left(1 - \rho\cos kL + i\rho \sin kL\right)}{(1-\rho)^2 + 4\rho \sin^2(kL/2)} \tag{2.14}$$

The complex argument gives the phase shift, which can be Taylor expanded around resonance ($kL \simeq 2\pi q$, where q is integer).

$$\arg F(k) = kd + \arctan \frac{\rho \sin kL}{1 - \rho \cos kL} \tag{2.15}$$

$$= kd + \frac{\rho kL}{1-\rho} + \mathcal{O}\left((kL)^3\right) \tag{2.16}$$

$$\simeq \frac{k(\overbrace{(1-\rho)}^{\simeq 0} d \; + \; \overbrace{\rho}^{\simeq 1} \; L)}{1-\rho} \tag{2.17}$$

$$\simeq \frac{kL}{1-\rho} \tag{2.18}$$

The extra term $\pi = \arg(-1)$ in the complex angle was omitted and $kL \simeq 2\pi q$

was assumed (close to resonance). We are only interested in dependence on small changes around $\omega_0 = \frac{kL}{\tau}$ (τ is the round-trip time). Therefore, any frequency-independent phase terms can be neglected. From this point, everything will be formally the same as for a linear cavity. It can also be shown that

$$F(k) = e^{i\left(kd-\frac{kL}{2}\right)} \underbrace{\left(-\sqrt{T}\frac{e^{i\frac{kL}{2}}}{1-\rho e^{ikL}}\right)}_{F(k) \text{ for linear cavity}} \tag{2.19}$$

and then $kd - \frac{kL}{2}$ becomes negligible again because of the $1-\rho$ factor. As a consequence, in this calculation only the circulating field has contribution, although the initial idea that we probe the cavity like a medium and measure the group delay between the input and output certainly sounds more intuitive. In conclusion, as long as we only want to estimate the overall phase shift of the transmitted field without worrying about interference effects where some small phase terms could matter, the unusual cavity geometry will not make this calculation harder. Finally, the group delay of the empty cavity is

$$\tau_g = \partial_\omega \left(\frac{\omega\tau}{1-\rho}\right) \tag{2.20}$$

$$= \frac{\tau}{1-\rho}. \tag{2.21}$$

The effective group index is given below.

$$n_g = \frac{\tau_g c}{L} \tag{2.22}$$

$$= \frac{\tau_g}{\tau} \tag{2.23}$$

$$= \frac{1}{1-\rho} \tag{2.24}$$

2.3.2 Effect of Medium

Suppose a uniform medium in the cavity, which will make the analytical formulas look simpler. Applying Equation (2.1), the exponential factor describing absorption or gain can be linearly approximated as long as $kL\,\mathrm{Im}(\chi(\omega)) \ll 1$, which considers the round-trip losses or gain. The previous method with the transformation

$$kL \;\rightarrow\; kL\left(1+\frac{1}{2}\,\mathrm{Re}(\chi(\omega))\right) \tag{2.25}$$

$$\rho \;\rightarrow\; \rho\left(1-\frac{1}{2}kL\,\mathrm{Im}(\chi(\omega))\right) \tag{2.26}$$

takes into account the medium in the cavity. These relations are valid when $kL\,\mathrm{Im}(\chi) \ll 1$.

$$n_g \;=\; \partial_\omega\left(\frac{\omega\left(1+\mathrm{Re}(\chi(\omega))\right)}{1-\rho\left(1-\omega\tau\,\mathrm{Im}(\chi(\omega))\right)}\right)\Bigg|_{\omega=\omega_0} \tag{2.27}$$

The transformation in Equations (2.25) and (2.26) make a connection between the Lorentzian susceptibility in Equation (2.6) and the empty cavity transmission function in Equation (2.14) so we can plot the power transfer function $\left|F(k)\right|^2$, phase, and group index of the cavity with a gain medium. Assume a Lorentzian gain peak with a width equal to the cavity linewidth, 0 detuning between the centre of the transmission peak of the empty cavity and that of the gain peak, and a peak gain that would lead to a decay of the electric field amplitude, with a time constant $-\kappa/4$ (increasing amplitude) if there was no cavity around it (described by only Equation (2.1)). $-\kappa/4$ is an arbitrary choice, because these equations are unable to describe the effect of the increasing circulating field on the gain medium, and therefore we cannot

eliminate all the round-trip losses as that would mathematically lead to an unstable system (physically it would require an infinitely strong pumping mechanism). In other words, now we only introduce some gain in order to reduce the round-trip losses without reaching the lasing threshold. As the round-trip losses are small in the experiment (for example, for the reflection coefficients used in the experiment $\rho = 0.99817$ in Equation (2.14)), it is also numerically challenging to reduce them even more if we do not rely on approximations that are only valid when very close to resonance. An amplitude decay rate of $-\kappa/2$ (κ is now FWHM) in the gain medium would compensate for all the round-trip losses and the denominator in Equation (2.14) would become $1 - 1 = 0$. Note that the amplitudes of different numbers of round trips can only be summed up when they decrease as the number of round trips increases. Using Equations (2.1) and (2.6), and the condition that the introduced susceptibility in the cavity adds an extra amplitude decay at the rate $-\kappa/4$,

$$\Omega = -\frac{\kappa^2}{2\omega_0} \tag{2.28}$$

where the minus sign describes gain. The exact value of ω_0 does not matter as long as it is an integer multiple of $\frac{c}{L} \times 2\pi$ as the round-trip time is $\frac{L}{c}$. The parameters used in the experiment are $T = 0.00116$, $\rho = 0.99817$, $d = 4$ cm, $L = 10$ cm, and the FWHM linewidth of the cavity (and now also the gain peak) is

$$\kappa = 2\frac{1-\rho}{\sqrt{\rho}}\frac{c}{L} = 2\pi \times 1.75 \text{ MHz} \tag{2.29}$$

as explained in [26], which can be derived by solving $\left|F(k)\right|^2 = \frac{1}{2}$. The plotted power transfer function, phase, and group index for the empty cavity and a weak (not lasing) gain medium are in Figure 2.5.

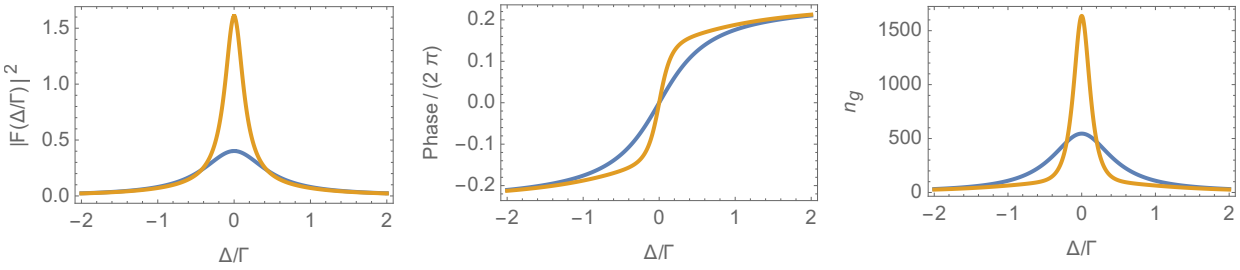

Figure 2.5 Comparison between the empty cavity (blue curve) and a cavity with a weak gain medium (yellow curve).

In conclusion, the empty cavity already behaves similarly to a slow-light medium with a large group index and a gain medium with a single gain peak can further enhance this effect. These formulas do not take into account anything that is not reflection or transmission, that is, any extra absorption and scattering caused by the cavity mirrors.

In homogeneously broadened media $\mathrm{Im}(\chi)$ has a Lorentzian feature and there is a cavity resonance close to the centre frequency. In this case, $\mathrm{Im}(\chi)$ is constant and $\mathrm{Re}(\chi)$ is linear. The above treatment of susceptibility is only valid if the medium is probed with a weak beam that has no effect on the medium itself. However, in lasers, due to depletion of the finite amount of input power the system can receive, the shape of $\mathrm{Im}(\chi)$ will be different once the threshold has been exceeded. This will be discussed in the next session.

Saturation and Frequency Pulling

This section will summarise how the susceptibility changes above threshold [29, 47, 48]. The cavity can be described as a medium with losses and Maxwell's equations combined with some approximations (e.g. neglection of higher order derivatives, products of derivatives) give the slowly varying

part of the electric field (as derived in [47, 48]):

$$\dot{E} = -\frac{1}{2}\frac{\omega}{Q}E - \frac{1}{2}\omega \operatorname{Im}(\chi(E,\omega)), \tag{2.30}$$

where $Q = \frac{\omega_q}{\kappa}$ is the quality factor of the cavity, ω_q is the cavity resonance frequency, and ω is the lasing frequency. Because of saturation of the gain medium, the susceptibility depends on the electric field as well. Let us start by writing the unsaturated susceptibility that has a single gain peak [48] (which is suitable for describing most applications)

$$\operatorname{Im}(\chi(\omega)) = -G\frac{\Gamma^2}{2\Omega^2 + \Gamma^2 + 4\left(\omega - \omega_0\right)^2}, \tag{2.31}$$

$$\operatorname{Re}(\chi(\omega)) = G\frac{2\left(\omega - \omega_0\right)}{\Gamma}\frac{\Gamma^2}{2\Omega^2 + \Gamma^2 + 4\left(\omega - \omega_0\right)^2}, \tag{2.32}$$

where G is the gain parameter, $\Omega = -\frac{\left\langle \hat{E}\hat{\mu} \right\rangle}{\hbar}$ is the Rabi frequency [29, 33], $\hat{\mu} = -e\hat{r}$ is the dipole operator, $\hat{E}$ is the quantised electric field (not used explicitly in this thesis), Γ is the FWHM of the gain peak, and ω_0 is the centre frequency of the gain peak. The gain medium can only provide a finite amount of power and suppose that the system reaches equilibrium (constant lasing power) above threshold. $\dot{E} = 0$ in Equation (2.30) leads to the following [48].

$$\operatorname{Im}(\chi(E,\omega)) = -\frac{1}{Q} \tag{2.33}$$

$$\operatorname{Re}(\chi(E,\omega)) = \frac{2\left(\omega - \omega_0\right)}{Q\Gamma} \tag{2.34}$$

$$\frac{2\Omega^2}{\Gamma^2} = QG - 1 - \left(\frac{\omega - \omega_0}{\Gamma/2}\right)^2 \tag{2.35}$$

ω is such that the gain allows the system to lase at that frequency (we will calculate the exact frequency shortly). $\chi(E,\omega)$ can be solved outside the

possible lasing frequencies as well and the Kramers-Kronig relations can be redefined [48]. From Equations (2.3), (2.5), and (2.34), the group index can also be calculated:

$$n_g = 1 + \frac{\kappa}{\Gamma} \tag{2.36}$$

We are now going to calculate the lasing frequency ω. Following [29] and recalling Equation (2.1), both the free-space propagation of the electric field and propagation through the dispersive medium contribute to the round-trip phase shift in a cavity:

$$\frac{\omega}{c}L + \frac{\omega}{c}\frac{1}{2}\,\mathrm{Re}(\chi(\omega))L_m = q2\pi, \tag{2.37}$$

where ω is the frequency of the cavity mode, L is the round-trip length of the cavity, L_m denotes the length of the gain medium, and q is an integer. Additional phase shifts (e.g. reflection from the mirrors and the Gouy phase for a realistic Gaussian mode) are now neglected. This equation describes the round-trip phase condition when there is a dispersive medium in the cavity. We can write $q2\pi = \frac{\omega_q L}{c}$ on the right-hand side of Equation (2.37), and use Equation (2.34) and $\omega_0 \simeq \omega_q$ as in practice the frequencies are large enough that only the linewidths differ in the quality factors of the cavity and the gain medium. $L = L_m$ is assumed (the gain parameter G can be rescaled accordingly). The lasing frequency is

$$\omega = \frac{\kappa\omega_q + \Gamma\omega_0}{\kappa + \Gamma}, \tag{2.38}$$

which is sometimes written in terms of quality factors of the cavity and the gain medium. κ is usually meant to be angular frequency and Γ is

the FWHM of the gain peak. However, when Equation (2.38) is applied, all the frequencies must have the same unit. Equation (2.38) gives the lasing frequency and (2.35) gives the lasing intensity as a function of lasing frequency.

Homogeneous and Inhomogeneous Broadening

How the gain behaves at different frequencies depends on the nature of the gain medium [4, 29]. In a homogeneously broadened medium, all parts of the gain medium provide the same gain peak. The gain peak of the whole medium decreases at all frequencies by the same factor. In moving atoms (gases) or vibrating lattices (solids) a given frequency can never deplete all the gain as the centre of the gain peak changes along the medium. The unsaturated part can sometimes reach the threshold of a lasing mode at another frequency unless there are extra losses at that frequency (e.g. a second cavity). This kind of medium is inhomogeneously broadened. Cold atoms at sufficiently low enough temperature are homogeneously broadened.

Chapter 3

Magneto-Optically Trapped ^{39}K Atoms

The magneto-optical trapping (MOT) design was explained in earlier theses [25–27]. The atom source and some parts of the laser system were replaced, which resulted in a higher atom number and a more stable setup. This chapter will give a short overview emphasising the improvements and changes.

3.1 Vacuum System

MOT experiments only work effectively in ultra-high vacuum, which usually means less than 10^{-8} mbar. This is because collisions with hot atoms and molecules of the background gas make the trapped atoms hotter and destroy the trap. The purpose of the vacuum system is to keep the pressure low, provide an atom source the experiment requires, and let the necessary optical fields traverse some parts of the system. After the system is assembled and sealed, it has to be baked, that is, pumped and kept at a high temperature to evaporate any contamination (usually water) stuck to the inner surface.

These were described extensively in [25–27], but some changes had to be made to the old system which means, a similar (although not so long and rigorous) procedure for pumping and baking was necessary in order to make sure the new components and joints were sealed completely.

The experiment works as follows. Potassium atoms are loaded from an ampoule and trapped in a 2D MOT chamber (2D MOT means 2 pairs of cooling and trapping beams without a third one) and a push beam (Figure 3.1) that goes along the long axis of the vacuum system. The push beam hits the atoms of the 2D MOT so that they can go through a graphite tube and get trapped in the 3D MOT chamber. The alignment is such that the 3D MOT overlaps with the smallest waist of the ring cavity, maximising the in-cavity atom number. More atoms means more gain in the resulting ring laser. The old system could produce an atom number of about 5×10^7, but that required great luck with the alignment and vapour pressure and was not achievable most of the time. As a comparison, the lasing threshold in atom number was measured to be about 6×10^7 (Chapter 4) with good atom-cavity overlap and no sign of lasing has been reported by previous PhD students who used potassium dispensers in the original setup. The dispensers were also ageing as they did not supply enough atoms any more and it seemed inevitable to replace them.

The upgrades and data of a short baking period will be shown in the next few sections.

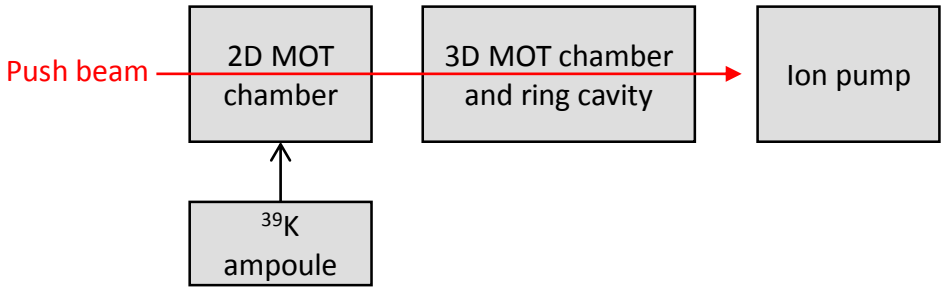

Figure 3.1 Simplified schematic of the experiment.

3.1.1 Upgrades to the Old System

The necessary modifications are listed in Table 3.1.

Proposed change	Main reason
A piece of Viton O-ring	Cavity vibrations
New imaging axis	Easier alignment of the 3D MOT
New atom source (ampoule)	No fluorescence in the new system

Table 3.1 Upgrades to the old vacuum system.

To allow for the new parts, some joints had to be replaced. In the end, only the MOT chambers and the nipple between them stayed in their old places, all the other components had to be removed, replaced, or reconnected (Figure 3.2).

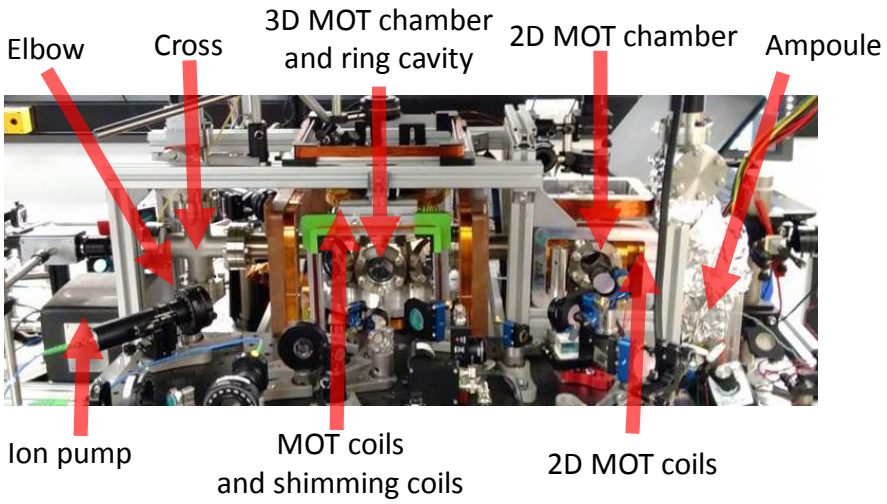

Figure 3.2 New experimental design.

3.1.2 New Atom Source

Atom Sources in General

As vacuum systems cannot be opened once at low pressure, the atomic species the experiment needs already have to be in the closed system. Whereas, it normally does not take long (a few hours to a few days) to find out whether the pressure is low enough, and everything is clean and sealed properly, atom sources work on a much longer timescale (a few weeks to a few months).

The two popular sources are dispensers and ampoules. Dispensers (Figure 3.3) contain much less material (a few mg), use a chemical reaction that gives byproducts, and do not release any atoms on their own (which could also be an advantage). Ampoules can only be controlled by their temperature once their glass seal is broken, but contain about 1 g of material, and can be considered pure when compared to dispensers.

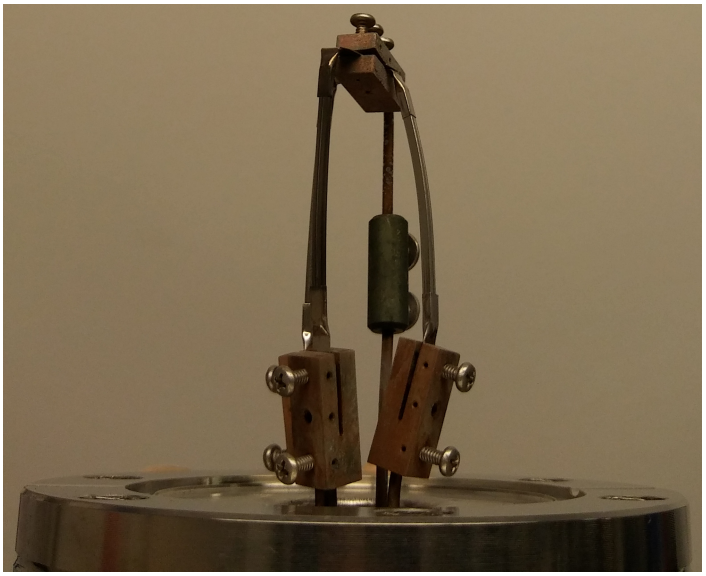

Figure 3.3 Three ^{39}K dispensers connected to a feedthrough. Only a small part of these thin rods is actually potassium.

Upgrades to the Old Atom Source

By design, the dispensers had to be heated (fired) by electric current to release atoms. The atom flux dropped after a few minutes and the current could only be turned back on after another few minutes. However, after baking the whole vacuum system, the dispensers had to be turned on many times to achieve a high enough vapour pressure as potassium tends to stick* to uncoated surface of vacuum components. They can become dirty when exposed to air after firing, which probably happened to ours in the new vacuum system, since there was no sign of fluorescence even after several weeks of firing dispensers. The new system was also bigger in volume and surface.

These issues went away when we started using an ampoule (Figure 3.4) as it could be left at a high temperature for a long time without super-

*This is not specific to potassium but a rather general phenomenon in this kind of experiments.

vision. With the ampoule kept around 90°C, it took about two weeks to coat the inner surface of the system with potassium and build up enough vapour pressure to see fluorescence. However, when the number of atoms in the MOT reached the target value (around 10^8 atoms) and did not seem to improve any more, the vapour pressure became more sensitive to the temperature of the ampoule. Unfortunately, sometimes the pressure could increase by 1-2 orders of magnitude even when there was no overall increase in temperature. The system cooled down a bit for a few days and returned to the same temperature, but after that the pressure was higher as if it had an effect opposite to that of baking. This happened sometimes over weekends or holidays due to temporarily reduced heating in the building. Even though it never actually interrupted the experiment, this problem was mostly resolved by switching off all the heaters of the vacuum system about 4 months after breaking the glass seal of the ampoule.

In overall, the ampoule was easier to work with than the dispensers, provided a cleaner source of ^{39}K, and finally the low vapour pressure of ^{39}K even became an advantage as the ion pump current slowly reached 0, which was never possible with the dispensers, when the ampoule was not heated. The overall low pressure (i.e. clean vacuum) could also be seen by how slowly the MOT built up and decayed* compared to the old system that used dispensers.

*This was only observed by eye and never measured due to lack of time and importance as the full characterisation and optimisation of the MOT were done by former PhD students [26, 27].

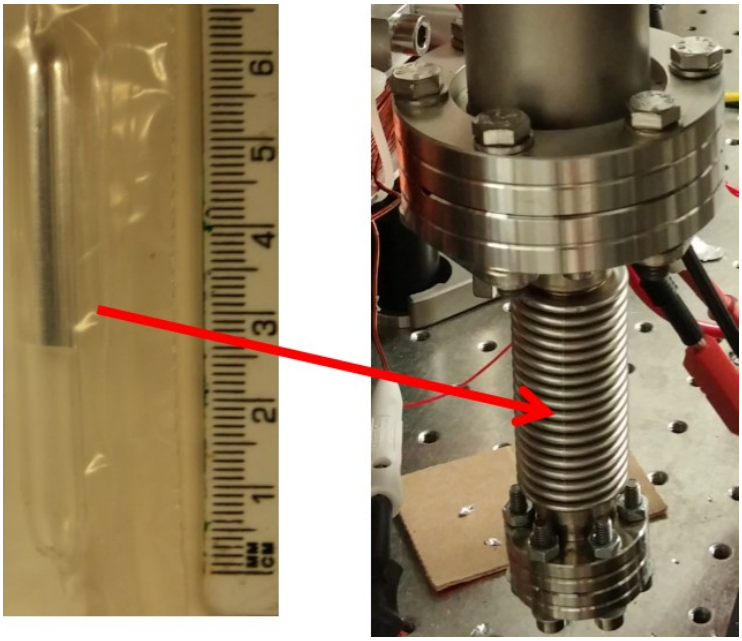

Figure 3.4 ^{39}K ampoule and its bellows. Bending the bellows broke the glass seal.

3.1.3 Baking the New Vacuum System

The new vacuum system was wrapped up and baked, but only for a few days, instead of a few weeks. The time-pressure diagram is shown in Figure 3.5. Because the 2D MOT chamber was normally heated (which means that the pressure was not uniform either) even when it was not baked, it started at a much higher temperature. The reason for the time gaps was that no measurements were made at night. The initial pressure was 2.5×10^{-8} mbar and it went down to 5.3×10^{-9} mbar after baking, which indicated that there were probably no leaks and the new system became clean enough.

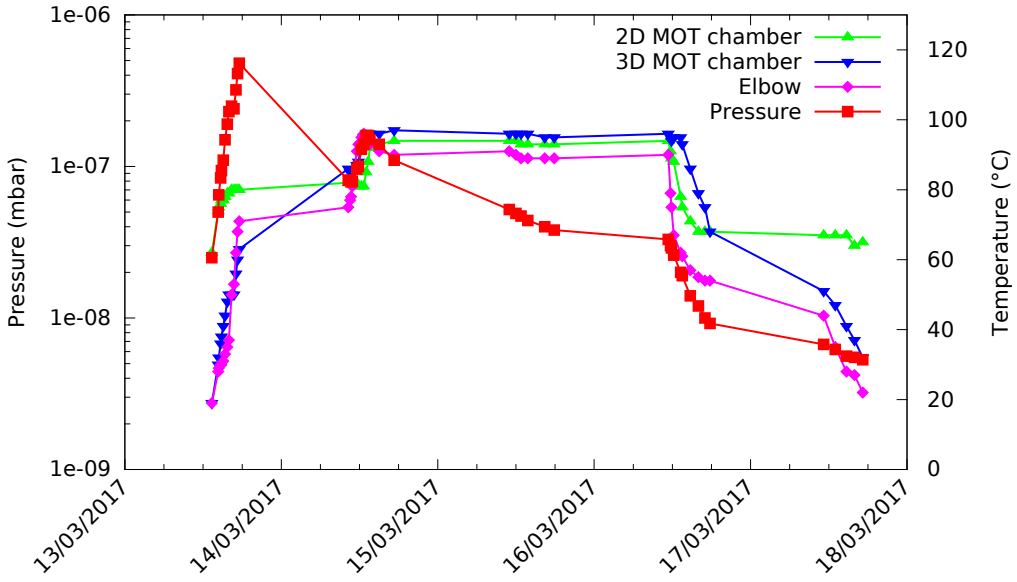

Figure 3.5 Pressure (red squares) measured by the gauge connected to the turbo pump and temperature (upward-pointing green triangles, downward-pointing blue triangles, and purple diamonds) of three different parts of the new vacuum system plotted as a function of time.

3.1.4 Ion Pump

The ion pump, which uses strong magnets and a high voltage (a few kV), can reach lower pressure than turbo pumps. As it only traps and does not actually pump, this kind of pump also has to be cleaned (baked) sometimes. The ion pump is usually turned on after baking, when everything is cooled down. It can be turned on at a relatively high pressure, but the high pressure increases the current, reduces the voltage, and slows down the trapping. Ideally, most of the material should be removed from the system and not trapped inside, and a low pressure achieved with the turbo pump means that leaks are much less likely.

Although the new vacuum system was much bigger and the ion pump was moved farther from the MOT chambers, the ion pump current stayed much lower, which was attributed to the cleaner atom source mentioned in

Section 3.1.2.

3.2 Laser System

3.2.1 D_2 Hyperfine Structure of ^{39}K

Magneto-optical traps (MOT) are used in order to cool and trap atoms. It is based on Doppler cooling. The atom moving towards an incoming red-detuned laser beam slows down when it absorbs a photon. This results in a friction force when applied in all directions (confinement in momentum space due to 3 pairs of retroreflected red-detuned cooling beams). The magnetic field makes this friction force spatially dependent (confinement in space). More detail on operation of a MOT can be found in other works [33, 38, 49, 50]. The same MOT configuration is described and characterised in [26, 27]. This section will briefly illustrate the energy levels of ^{39}K that are used in the experiment. Apart from the fact that there are separate 2D MOT and 3D MOT chambers, they run accordingly to the standard technique.

Each atomic species needs different MOT beam frequencies and intensities, because the energy level structure is different. Our 2D and 3D MOT configurations have mostly been built and studied by earlier PhD students [25–27]. In ^{39}K, the optimised laser frequencies relative to the hyperfine energy levels are shown in Figure 3.6. The hyperfine selection rule $\Delta F = 0, \pm 1$ implies that a single frequency would pump all the atoms from $F' = 0, 1, 2$ into $F = 1$, which could only be accessed by another beam at a different frequency, which is called the repump beam.

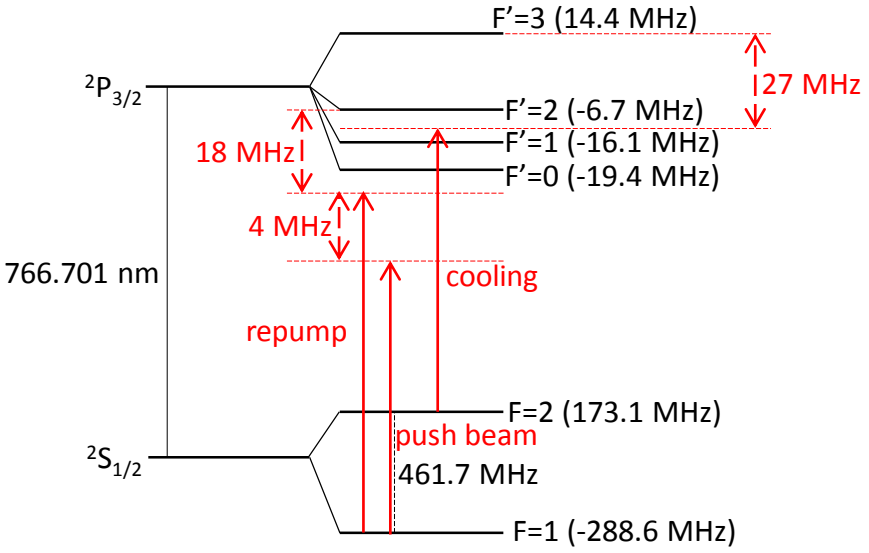

Figure 3.6 The D_2 line of ^{39}K and the hyperfine structure [51]. The transitions and detuning frequencies used for laser cooling are shown by red lines. The push beam is weak (about 0.7 mW and 1 mm of diameter) and misses the MOT so it has no role in cooling. It is only used for bringing atoms from the 2D MOT to the 3D MOT.

3.2.2 Overview of Laser System

The main upgrade was replacement of the old tapered amplifiers (TA). The rough schematic of the MOT laser system is shown in Figure 3.7. A ^{39}K vapour cell was set up for magnetically-induced dichroism spectroscopy [52] in order to lock [53] the master laser to a reference. The push laser was offset locked to the master laser and the cooling laser was offset locked to the push laser. An acousto-optical modulator (AOM) [54] generated the repump frequency, using some of the cooling power. The cooling laser provided around 50 mW, which, after the AOM and an isolator, was attenuated down to $12-16$ mW when it reached the TA. This was enough to seed the TA and obtain sufficient power for the MOT beams. Depending on the alignment, each 2D MOT beam had $100-150$ mW, and there was $20-30$ mW for each

3D MOT beam.

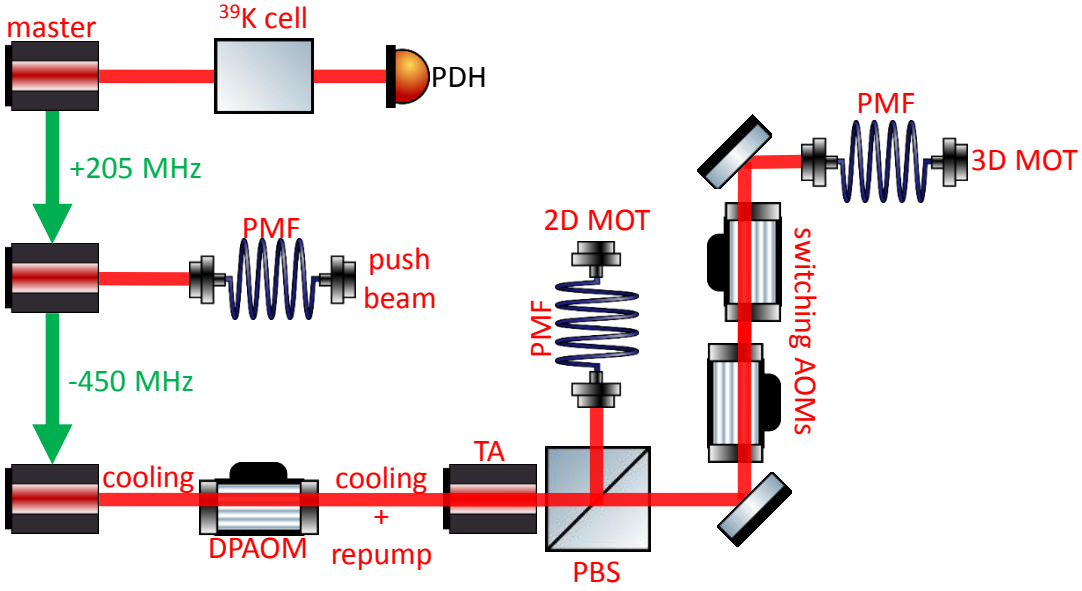

Figure 3.7 Simplified schematic of the MOT laser system. The green arrows denote beat note offset locks (only the frequencies are shown). PDH: photodiode for Pound-Drever-Hall frequency stabilisation [55, 56], PMF: polarisation maintaining optical fibre patch cord and couplers, (DP)AOM: (double-pass) acousto-optical modulator [54], PBS: polarising beam splitter, and TA: tapered amplifier.

The beat-note frequencies of the push and cooling lasers, and the AOM RF frequencies and powers were controlled by an experiment computer. This provided the opportunity to separately change the laser lock points, cooling and repump frequencies and powers, and switch or attenuate the 3D MOT beams.

3.2.3 New Tapered Amplifier Design

In order to keep the experiment working, it was necessary to replace the old amplifier system. The advantage of the new tapered amplifier (TA) was that there were no movable or adjustable optics or connectors, and everything (including cables and electronics) was glued or soldered (Figure 3.8). During

one year of operation, it never had to be opened. Sometimes there seemed to be a slight drift in collimation, but that could be fixed by aligning the surrounding lenses outside the TA. On both sides of the amplifier chip, there were an aspheric lens, cylindrical and spherical telescopes. After the aspheric lens at the output, the beam was nearly collimated vertically, but was astigmatic because of the wide numerical aperture of the output facet of the chip. In order to correct for this, there was an additional cylindrical lens. This was not a big issue in the earlier design, which produced about half as much power, had a smaller output aperture, and therefore it was also less multi-mode.

In total, an aspheric lens, three cylindrical lenses and a spherical telescope were needed after the output of the chip in order to couple enough light into the MOT fibres. The coupling efficiency was about 28% (560 mW in the fibres out of about 2000 mW measured at the chip), which also includes losses to lenses, waveplates and an isolator. Another commonly used technique is to put an iris in the focused beam, which filters the light in Fourier space, although the combination of lenses and irises that were available did not lead to nearly as much power in the fibres.

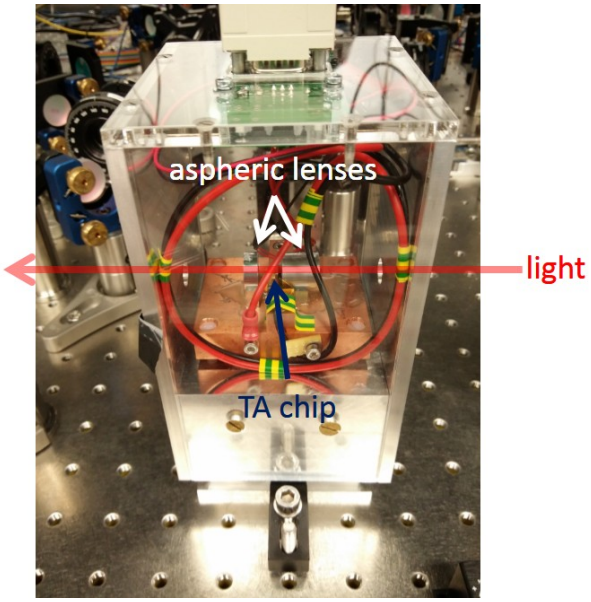

Figure 3.8 New TA design in the experiment. The amplifier chip was in the centre. There was a Peltier module for temperature control between the small copper and large aluminium blocks. A small piece of black paper on the output side was blocking a small amount of light back-reflected by lenses.

The alignment of the input was much easier because of the small aperture. With the cylindrical and spherical telescopes, the input beam was mode-matched and aligned to the back-reflected amplified spontaneous emission of the TA. This was necessary to exceed the minimum specified seed power of 10 mW and achieve enough output power (Figure 3.9). The recommended maximum power (2000 mW) was reached below the maximum driving current (4000 mA). There were only very small jumps (mode hops) in power, although the temperature control did not always have enough time to stabilise during the measurement.

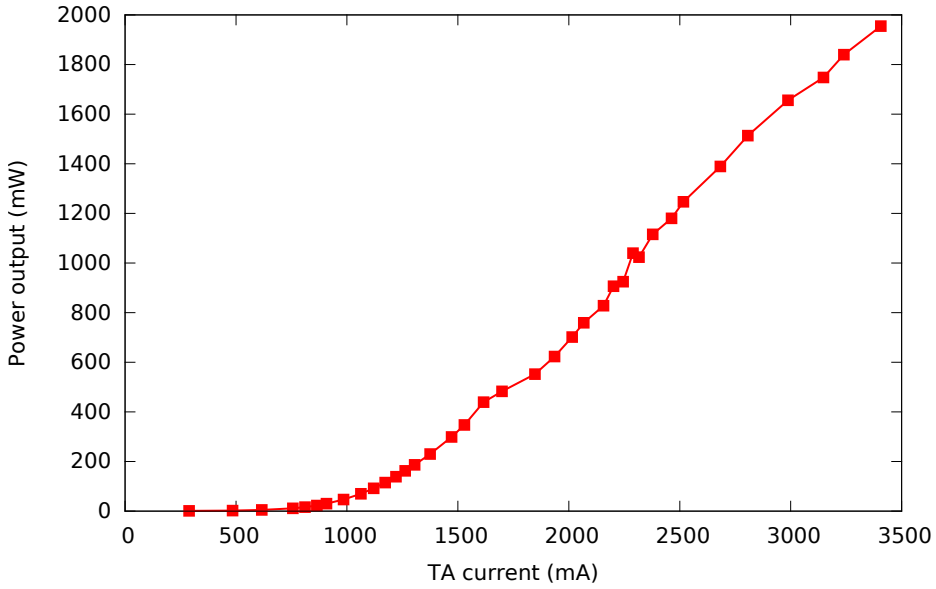

Figure 3.9 TA output power as a function of driving current for 15 mW of seed power.

The ideal cooling:repump ratio could only be achieved by optimising the alignment of the TA input and the RF power sent to the repump AOM, even though the target range of values (between 3 : 2 and 2 : 1) that gave a high enough atom number in the MOT (around 5×10^7) was found by previous PhD students. Therefore, this had to be measured again (Figure 3.10). A fraction of the TA output was sent through the science cavity and the transmission was measured. Changing the RF power revealed which peaks were at the cooling and repump frequencies. The other peaks were assumed to be different transverse modes and/or spontaneous emission from the TA.

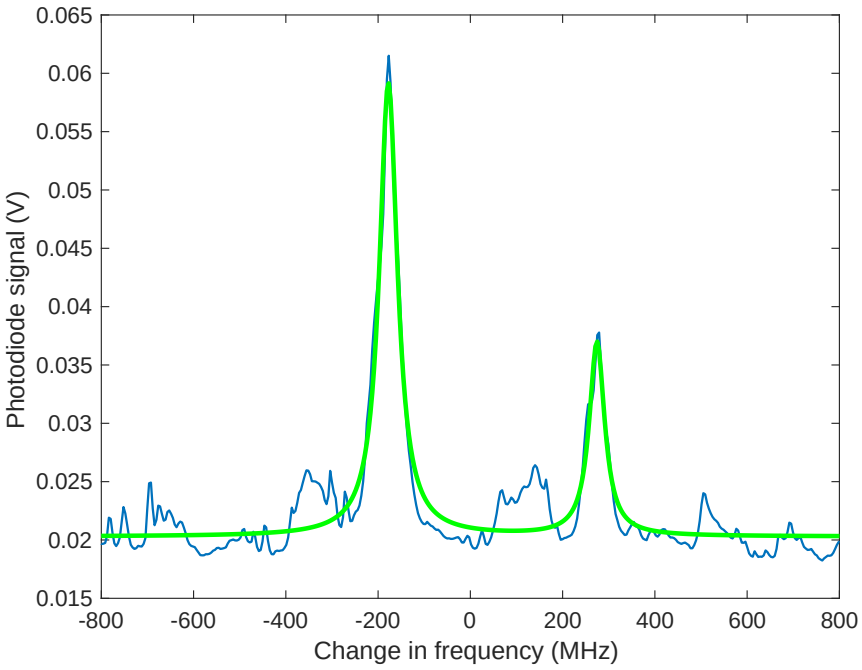

Figure 3.10 Ratio of cooling to repump power after the TA. The bigger green peak is the cooling and the smaller one is the repump. The frequency scale was given by the RF frequency of the repump AOM. The FSR of the cavity was about 3 GHz.

3.3 Coils and Magnetic Field

The original set of coils was built to provide an elongated 3D MOT overlapping the cavity mode [25, 26]. However, the atom number was never really as high as expected and the alignment of the MOT (angle and position with respect to the cavity mode) also proved to be difficult. Therefore, in the new version of the experiment a simple anti-Helmholtz geometry was utilised (Figure 3.11). Figures 3.12 and 3.13 show the theoretical prediction and the measured gradient along the strong axis. The target value was around 10 $\frac{\mathrm{G}}{\mathrm{cm}}$. The measurement of the gradient was performed at 0.64 A and gave (0.698 ± 0.0075) $\frac{\mathrm{G}}{\mathrm{cm}}$, which would be 10.91 $\frac{\mathrm{G}}{\mathrm{cm}}$ at 10 A. The inner

diameter of each coil was 11 cm and the separation of the two coils was 12 cm. The 2D MOT coils had 222 turns of round wire [26] and the 3D MOT coils had 68 turns of Kapton-insulated ribbon wire with a flat cross section of 1.2 mm $\times$ 0.2 mm. The final separation and current of 3D MOT coils were about 15 cm and 12 A in order to allow for extra shimming coils (not shown in the pictures) as well. Figure 3.12 tells us that the same gradient can be obtained for a larger separation and a slightly higher current.

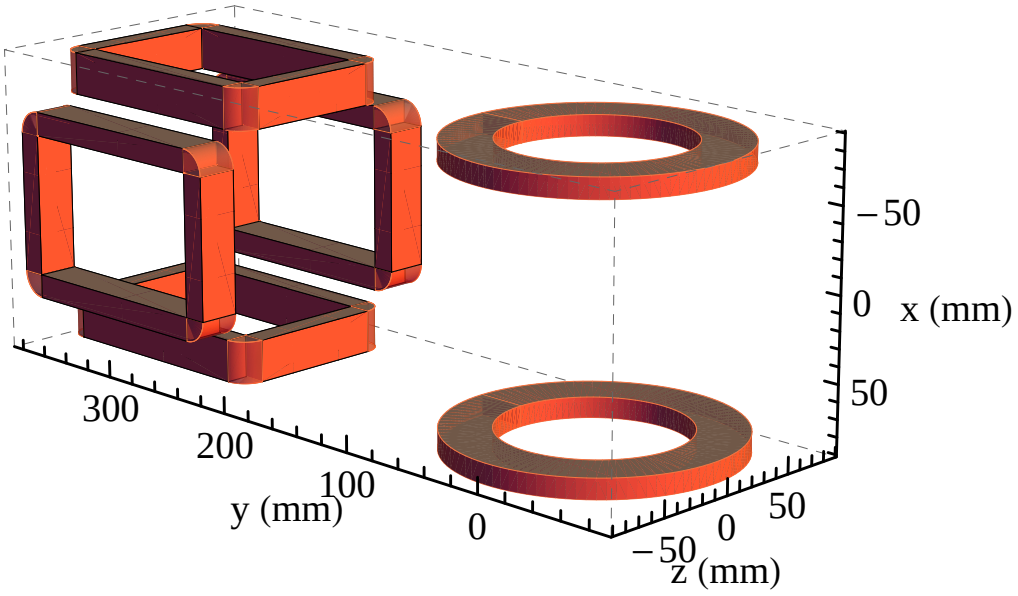

Figure 3.11 2D MOT (left) and 3D MOT coils (right).

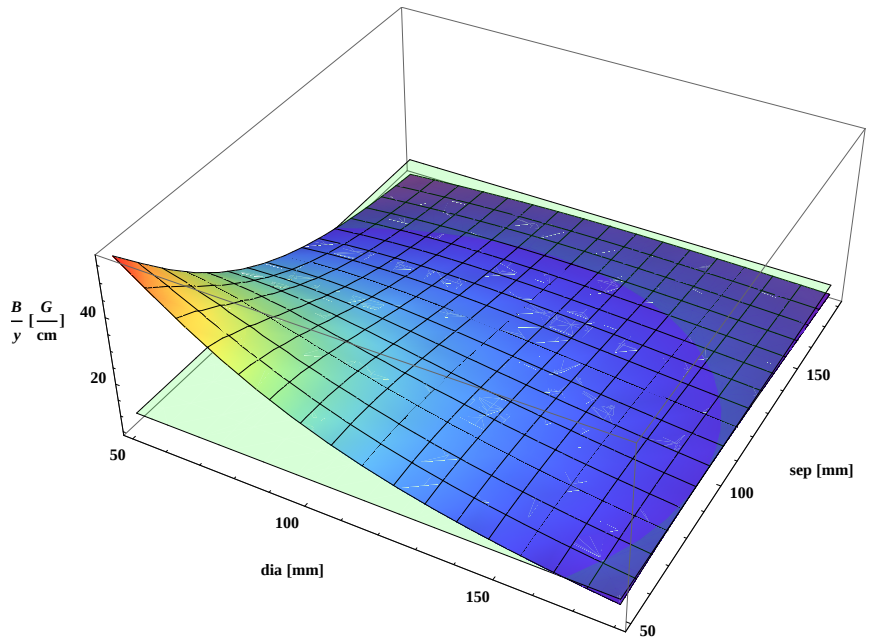

Figure 3.12 Simulated gradient of the 3D MOT coils as a function of coil diameter and separation. The aim is 10 $\frac{\mathrm{G}}{\mathrm{cm}}$, which is indicated by the light green surface. The parameter combinations that result in a gradient above the light green surface are suitable for our MOT.

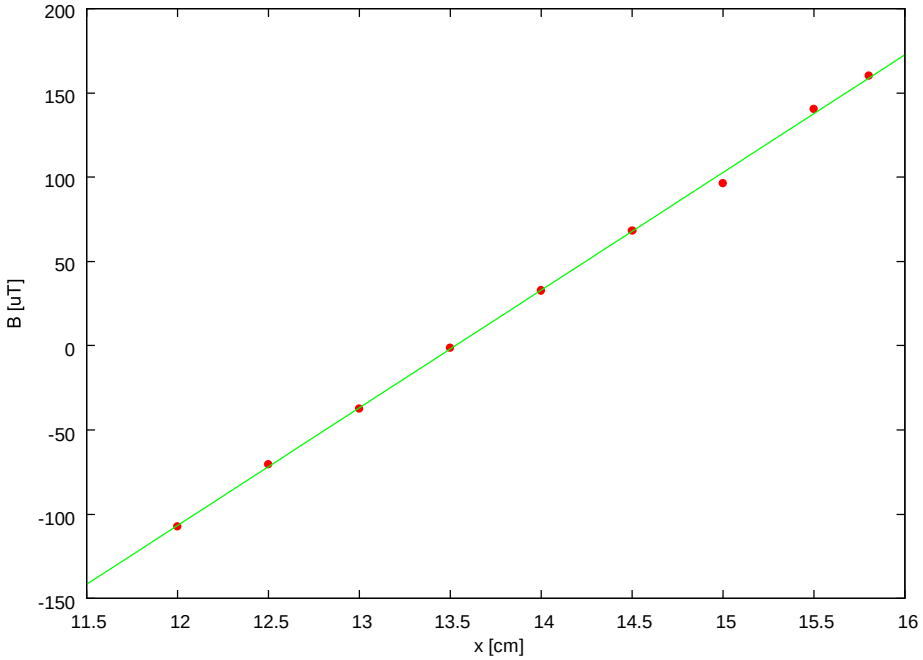

Figure 3.13 Measured magnetic field of the 3D MOT coils along the strong axis. The red dots are data and the green line is a fit. The slope is $(69.8 \pm 0.0075)\ \frac{\mu T}{cm}$. The offset on the x axis was only an arbitrary point on the translation stage where measurements were possible and the displacement of the translation stage was measured. The geometric centre could not be determined accurately in that setup. The biggest source of error was stray magnetic field from the optical table and the environment, which was not characterised as this measurement was performed on a different optical table and not in the real experiment.

3.4 Measurements

The measured quantities usually include atom number, temperature, and cloud size/aspect ratio. The MOT beam intensities and frequencies, coil currents, push beam alignment and intensity were then optimised for the desired values. These were explained in [25–27]. In this project, the key parameter was the optical depth, which was, in practice, maximised by optimising the in-cavity atom number. A higher total atom number gave a higher in-cavity number (there was usually a factor of a few hundred between the two numbers and this ratio seemed to increase for higher total atom

number). A higher in-cavity atom number means a larger gain medium and the whole MOT has more contribution to optical gain of the cavity mode.

The total atom number was measured by taking pictures of the MOT with a calibrated camera, and using a 6-level model [26, 57] and the experimental parameters (laser beam detunings and optical powers). The typical atom number was around 10^8 and it was reliably achievable in the new setup. It could be lowered by the push beam and MOT beam intensities for measurements. The cloud size was usually slightly below 1 mm with an aspect ratio close to 1:2 (based on the pictures). The temperature was on the order of mK in a running MOT. It was never measured during my final year, but earlier students used release and recapture method (turning off the MOT beams for a controlled period of time and taking pictures of the MOT initially and after recapturing some atoms). The in-cavity atom number could only be determined accurately by performing measurements on the atom-cavity system, but generally it was a few hundred times less than the total atom number. The atom-cavity overlap was controlled by shimming coils (2 pairs for each of the 3 dimensions) and beam alignment.

Figure 3.14 shows the 2D MOT and around 4×10^8 atoms were calculated from Figure 3.15, using the same method as in earlier theses [25–27].

Figure 3.14 2D MOT recorded as the camera was facing the nearest viewport. The push beam was blocked.

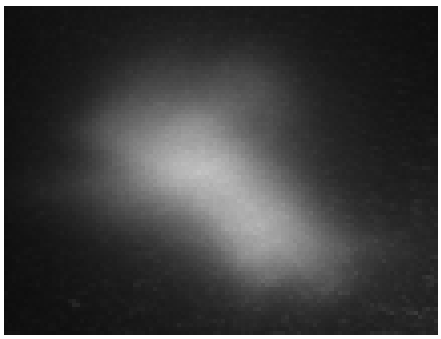

Figure 3.15 3D MOT. 4×10^8 atoms.

Chapter 4

Magneto-Optically Trapped ^{39}K Atoms in a Ring Cavity

The gain medium was described in Chapter 3. This chapter will lay out what had to be done in order to construct a feedback mechanism, that is, how the cavity and the gain medium were combined. This will be followed by some measurement data of the operating laser.

4.1 Ring Cavity

Standing-wave cavities with two mirrors are not suitable for ring lasers, but three mirrors suffice. This type of ring cavity was used for feedback in the final measurements. The next few sections will not deal with the atoms and only introduce the details of the ring cavity design and the relevant optical systems. There has been some advancement of the surrounding optics, although the cavity mirrors themselves have not been touched since the last two theses [26, 27].

4.1.1 Dimensions and Parameters

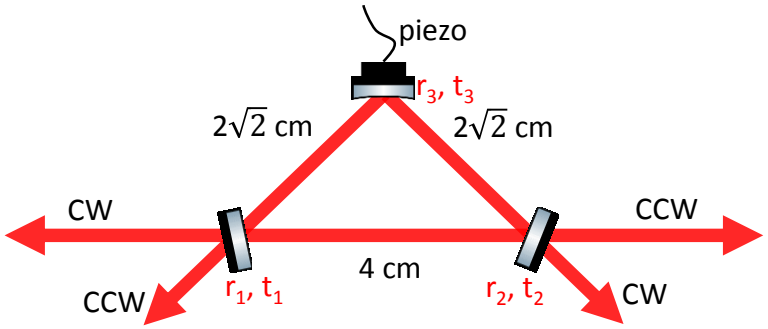

Figure 4.1 The ring cavity with the piezo and two counterpropagating clockwise (CW) and counterclockwise (CCW) modes.

The scale and simplified design of the ring cavity is shown in Figure 4.1. The most important quantities are listed in Table 4.1. With the piezo voltage the cavity length could be scanned just over a full free spectral range. The linewidth could be measured by probing the cavity around a resonance peak. The PDH sidebands give the scale that can be used to estimate the linewidth. A more acceptable method is cavity ring-down measurement (although this was not done during my time), which measures the exponentially decaying output power after the input beam is switched off by 2 AOMs that are aligned to opposite orders (no overall frequency shift) and provide a switching time of a few 10 ns. The power decay rate is twice the HWHM linewidth in angular frequency units. The biggest source of error was the initial delay caused by the switching. The cavity length and FSR were measured by scanning the piezo across different higher-order transverse modes [26, 58]. The PDH sidebands provided local frequency calibration. The linearity of the piezo scans was worse for large scans. The waists were calculated based on the mirror parameters.

Linewidth (HWHM)	920(30) kHz
Round-Trip Length	9.51(5) cm
Radius of Curvature of Central Mirror	10 cm
Sagittal Waist	128.0(3) µm
Tangential Waist	90.2(5) µm
Free Spectral Range	3151(16) MHz
Finesse	1710(60)
Round-Trip Losses	$\lesssim 0.4\%$

Table 4.1 Ring cavity parameters.

When the magnetic field of the MOT coils was attempted to be switched off suddenly, the round-trip cavity length suffered from small oscillations at around 1.8 kHz, which were greatly reduced by a piece of Viton (Figure 4.2), but never completely disappeared. The whole vacuum system was designed to be a rigid block in order to sustain the tight alignment constraints of the high-finesse cavity, which, together with the 1-mm-thin metal plate between the piezo and the curved cavity mirror, were assumed to be responsible for lack of mechanical damping. In practice, a cavity scan took at least a few ms over a few FWHMs and sometimes 10s of ms over a larger range. These did not cause any significant issues to the measurements as it was possible to avoid having to switch off the magnetic field. There is a balance between good vibrational isolation, and the freedom or stability of optical alignment.

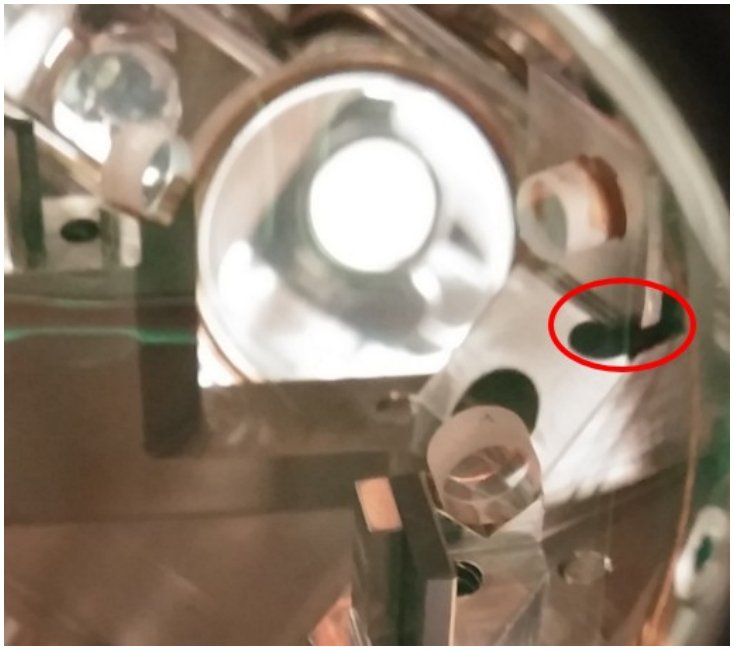

Figure 4.2 The upgraded ring cavity with some damping. The piece of Viton is inside the red circle.

4.1.2 Laser System

The next two sections will outline what was necessary to make measurements with the ring cavity. More detail can be found in [24, 26]. The main focus will be on recent improvements.

Overview of the Ring Cavity Laser System

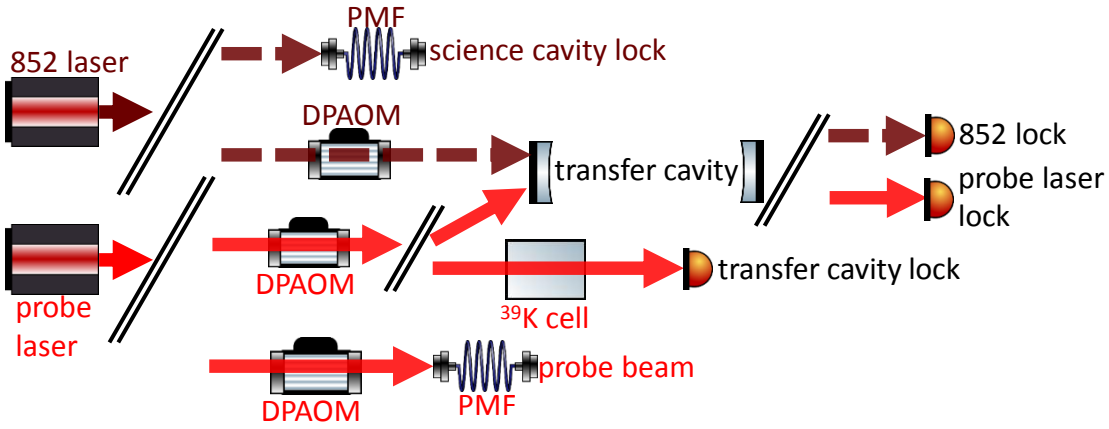

Figure 4.3 Simplified schematic of the probe laser system. The 852-nm laser (dashed brown lines) gives a far-off-resonant beam, which, in this setup, is only used to lock the science cavity (not shown). DPAOM: double-pass acousto-optical modulator and PMF: polarisation maintaining optical fibre patch cord and couplers. The ^{39}K cell is set up for frequency-modulation spectroscopy [59].

The MOT laser system was described in Section 3.2. Additional optical fields are needed to stabilise and probe the cavity-MOT system. This laser system is illustrated in Figure 4.3. The probe laser can be tuned to both D_1 and D_2 lines of ^{39}K and the frequency-modulation spectroscopy (FMS) [59] gives useful lock points in both cases. The chains of feedback loops, in which the last element provides the reference, were the following:

$$\text{probe laser} \rightarrow \text{transfer cavity} \rightarrow \text{FMS}$$

$$\text{science cavity} \rightarrow \text{852 laser} \rightarrow \text{transfer cavity}$$

The transfer cavity resonance at 852 nm and the RF frequency of the corresponding AOM were chosen so that the science cavity could be resonant with the atoms.

Upgrades to the Old Ring Cavity Laser System

The locking system (Section 4.1.2) only went through some minor modifications and optimisation, but the old cavity optics had to be extended in order to detect both clockwise (CW) and counterclockwise (CCW) travelling-wave modes, and their transverse patterns (Figure 4.4).

A flip mount with a big mirror could switch between detection of only the optical power or the transverse patterns. A beam splitter could have been an alternative solution, but, in that case, some optical power would have been wasted and the beam splitter would have disturbed the coupling into the optical fibres. Avalanche photodiodes* were used in order to detect the transmitted power for alignment purposes, but only single photon counters† had enough sensitivity and time resolution for most of the measurements (see Chapter 5). The beam profiler‡ could detect both optical power and transverse intensity distribution, but had a much lower bandwidth (the shortest exposure time that was used was 1 ms).

The CW fibre could be aligned to the transmitted probe beam. However, the CCW cavity mode was not probed. Instead, some light was injected into the CCW fibre and a photodiode was temporarily put on the other side of the cavity, where 852 nm was normally detected. The output of the CCW fibre was aligned to maximum transmission through the cavity and, because the high-finesse cavity already constrained the alignment, only required some small adjustments to optimise the coupling of the CCW cavity mode into its fibre, which was done when the cavity-MOT system started to lase (Chapter 5) and no probe beam was used.

*Laser Components LCSA500-03 APD
†Perkin Elmer SPCM-AQRH-13-FC
‡Thorlabs BC106-VIS

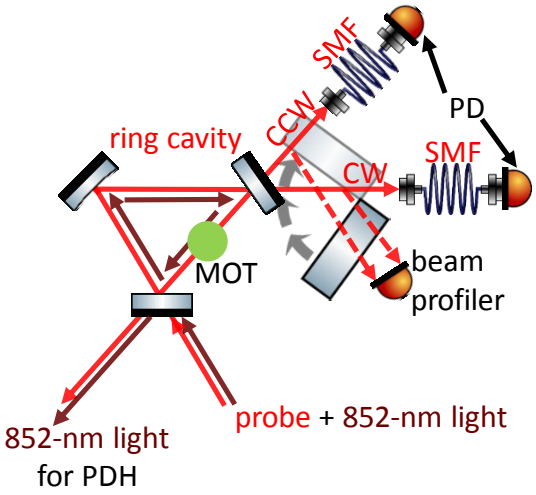

Figure 4.4 Upgrades to the cavity optics. PD: power detection (photodiodes or photon counters), and SMF: single-mode optical fibre patch cord. Long-pass and short-pass filters (not shown) were still used to block either of the two wavelengths.

4.2 Alignment and Strong Coupling

The work and measurements presented in this section did not directly lead to new results, but are meant to provide a smooth transition between the technical details of the upgrades showed in the previous sections, and the main results of the project (Chapter 5). Strong coupling in the old system was demonstrated in [26, 27, 58] so only an overview will be given in order to put the reproduced results in a new context, that is, the last prerequisite to lasing.

4.2.1 Optimisation of the MOT Position

The magnetic field affects the shape of the MOT and the atom number when nothing else is changed. In addition, to observe any interaction between the cavity mode and the atoms, they have to be in the same place. The shimming coils (Section 3.3) were able to smoothly move the position of $B = 0$, where the MOT lived, and based on the currents and directions, the position of the

MOT coils was corrected. The aim was to iteratively minimise the current in the shimming coils and only use the MOT coils, but a small current was still acceptable as all the coils could be left on during the measurements presented in this thesis. The alignment of the optics was such that the best MOT could only be achieved when it was in the smallest cavity waist (in practice, this also required some iterations). The shimming coils and the new imaging axis made this procedure much quicker than the old version of the experiment.

The MOT was moved as close to the cavity mode as possible, and with the right position of the MOT and frequency of the probe beam, the shape of the MOT (Figure 4.5) was changed by the cavity mode and the MOT also changed the cavity transmission spectrum (Section 4.2.2).

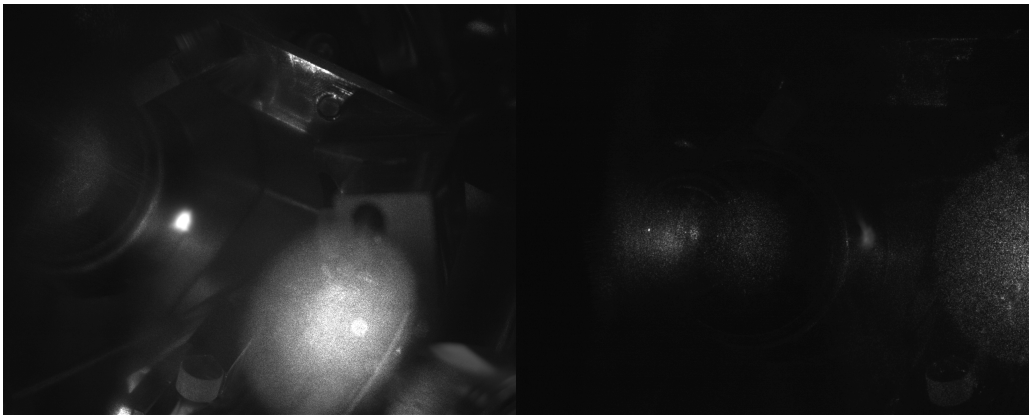

Figure 4.5 Left: 3D MOT in the ring cavity. Right: the first step to move the MOT to the right place. The pictures were taken on different days with different camera settings, but can still illustrate what it is like to work with atoms and cavities at the same time. The MOT was roughly 10 times larger than the smallest cavity waist.

4.2.2 Rabi Splitting

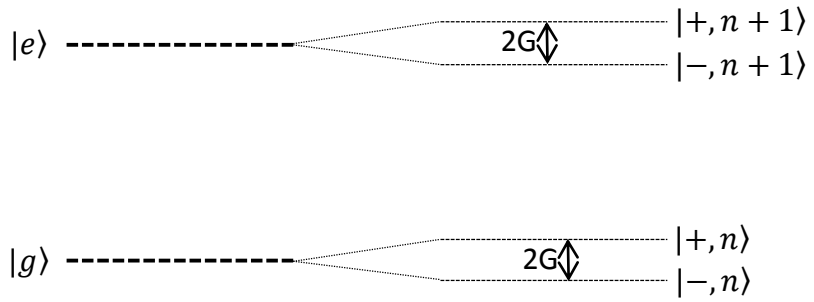

Figure 4.6 Bare atom energy levels and the atom-cavity system. The energy levels are split by twice the coupling constant g describing the interaction strength between the atom and the cavity mode.

Many atoms can also lead to strong coupling even when the single-atom coupling g is weak, which is called collective strong coupling (when N is large enough). It scales as $G = g\sqrt{\xi N}$ (ξ is the relative transition strength when multiple hyperfine levels are involved). When enough atoms are in the cavity mode, the interaction between the atoms and the cavity mode causes the free energy levels (2 atomic states and 1 photonic state for each photon number) to split [26, 27, 38, 58], which is called the Rabi splitting (Figure 4.6). If we use the two-level atom susceptibility as we did in earlier chapters, with a Lorentzian shape

$$\chi(\Delta) \propto -\frac{\Omega}{2}\frac{1}{\Delta - i\Gamma/2}, \tag{4.1}$$

where Δ is the probe-atom detuning, and Ω is the Rabi frequency of the probe beam, and probe the atom-cavity system, the cavity resonances split as Ω is increased (Figure 4.7). This can be seen by substituting Equation (4.1) into Equation (2.12), and using (2.25) and (2.26). $|F(k)|^2$ gives the transmission spectrum normalised to the incident power and the splitting

between the two side peaks is $\sqrt{\omega\Omega}$ [60] when the linewidths of the cavity and medium (Im(χ)) are the same (not true in the experiment, but it is easier to understand). The cavity-atom detuning is now 0. $\Omega = \frac{\Gamma^2}{\omega_0}$ describes an extra power decay at a rate Γ according to Equation (2.1), which helps us set the scale.

Experimental data is shown in Figure 4.8. The cavity was aligned to the D_1 $F = 1 \rightarrow F' = 2$ transition (not used anywhere else in this thesis) and the atom-cavity system was probed. The weak probe beam (on the order of 1 nW) was scanned across the peaks. The MOT was displaced by shimming coils in order to vary the in-cavity atom number. Rabi splitting was the best option to measure the in-cavity atom number as the MOT shape was also changing. Data in panels (b)-(d) give $7.47(6) \times 10^3$, $2.04(2) \times 10^4$, $4.9(15) \times 10^4$ atoms, respectively. The single-atom coupling was $g = 2\pi \times 91.5(5)$ kHz and the transition strength was $\xi = 5/18$. The cooperativity for (d) was $C = G^2/\left(\frac{1}{2}\kappa\gamma\right) = 58$ ($\frac{1}{2}\kappa$ is the cavity HWHM linewidth and $\gamma = 2\pi \times 2.978(6)$ MHz is the natural atomic HWHM linewidth). There is more explanation in [26, 27, 58].

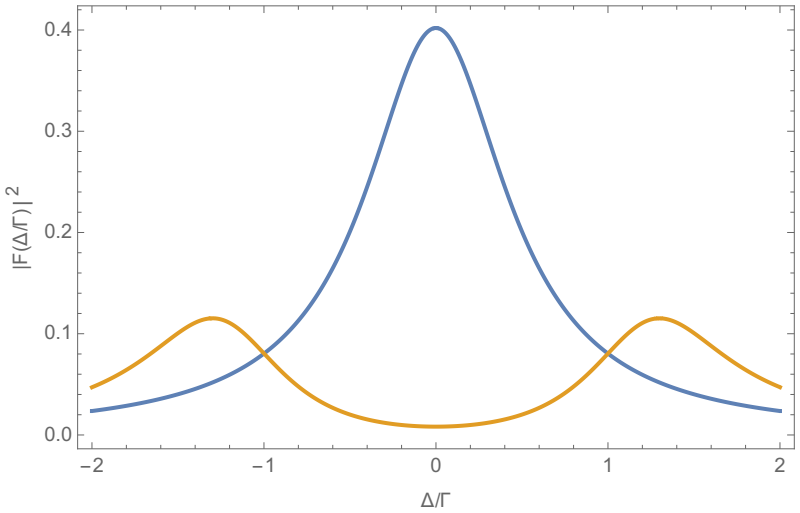

Figure 4.7 Rabi splitting (yellow curve) for $\Omega = \frac{6\Gamma^2}{\omega_0}$ (arbitrary choice). The blue curve shows the empty cavity. The cavity-atom detuning is 0.

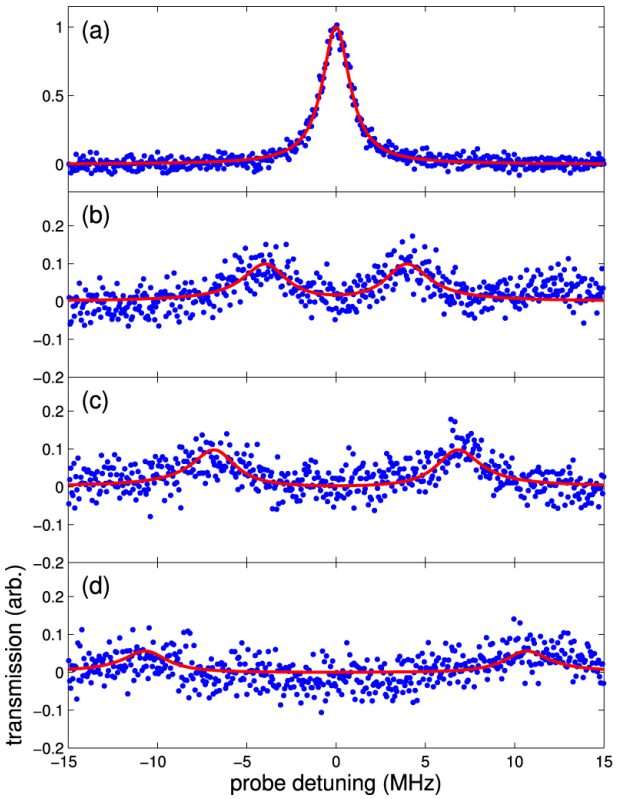

Figure 4.8 Rabi splitting for increasing atom number. Red: fits to the data. Blue: measurements. This picture was taken from [58].

The MOT could further be optimised by maximising the Rabi splitting. The D_1 line of potassium was used for Rabi splitting in earlier works and optimising the MOT before the main measurements, but it was not used afterwards. Although, in general, observation of strong coupling on one transition is not necessary in order to achieve lasing on another transition, due to how the experiment was set up, this* was a straightforward way to maximise the number of atoms interacting with the cavity mode.

*Increasing the in-cavity atom number was anticipated to increase the gain as well and since we did not see lasing at that time, reproducing some earlier results seemed essential in order to make sure everything in the new experiment was working well.

Chapter 5

Bidirectional Ring Laser

This chapter will summarise the main results of the experiment. Bidirectional lasing with magneto-optically trapped ^{39}K atoms in a ring cavity was characterised in four steps. The continuously running MOT showed a gain peak red detuned from the MOT cooling frequency. The cavity emitted output light in both directions in various transverse modes. Second-order coherence of lasing light was confirmed when operating above threshold, but fluorescence light below lasing threshold exhibited bunching and super-Poissonian statistics as expected. Finally, coming back to both directions, the counterpropagating cavity modes were uncorrelated but nonreciprocal in cavity length, that is, there was a splitting in optimum cavity length, between the output spectra of the two travelling waves.

5.1 Mollow Gain in ^{39}K Atoms

While lasing can involve a wide range of phenomena and it would be difficult to strictly define a list of requirements[†], there is no lasing without a gain

[†]For example, a cavity and population inversion are usually mentioned but not vital in general [35–37, 39, 40].

medium and a pump mechanism. This section will describe a gain mechanism (see Section 2.2 for a theory overview) that occurs in a continuously running ^{39}K MOT, which plays the role of a gain medium, and uses the MOT cooling beam as a pump beam.

5.1.1 Gain Measurement

Gain Measurement Procedure and Data

To obtain some information on the gain medium itself, feedback was avoided during the gain measurement in order to rule out any influence the lasing mode could have on the gain medium. For this purpose, the MOT was moved outside the cavity. A probe beam on the D_2 line, close to the MOT cooling frequency, was aligned* to hit the MOT and leave the 3D MOT chamber, but as opposed to what Section 4.2.1 described, both the MOT and the new probe beam had to miss the cavity mode and mirrors. Around 60 μW of incident power was used for alignment (Figure 5.1), but reduced to a few μW for the actual gain measurement (Figure 5.4). The single-pass gain had to exceed the round-trip cavity losses ($\approx 0.4\%$) in order for the system to lase.

*This is to clarify that the probing technique applied here was different to what was used in Section 4.2.1 and earlier works [26, 27, 58]. It was not meant to seed or inject the actual laser either.

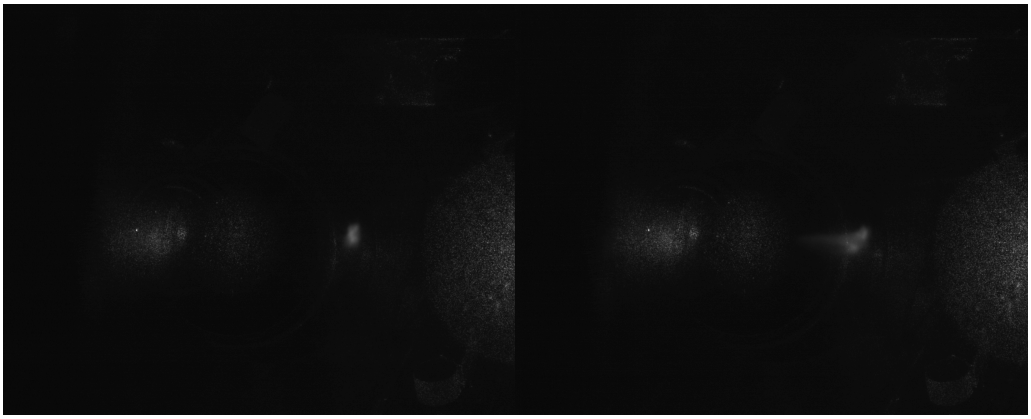

Figure 5.1 Left: 3D MOT under normal conditions. Right: 3D MOT distorted by the probe beam coming from the right side. This proves that we were probing the MOT.

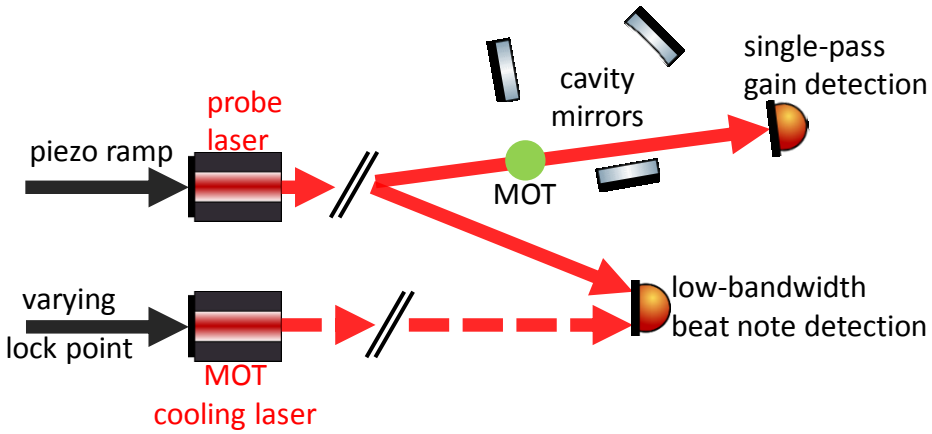

Figure 5.2 Simplified schematic of the gain measurement.

The probe beam was scanned across the D_2 hyperfine states and part of the same beam was beaten against a fraction of the MOT beam (Figure 5.2). The bandwidth of the beat-note photodetector was 300 kHz to mark the cooling frequency in the spectrum. No gain features were observed near the repump transition. The probe laser piezo was scanned across the static cavity and PDH modulation sidebands were used for calibration as a fraction of the same probe beam with added modulation was transmitted through

the empty ring cavity* (Figure 5.3). The MOT was not characterised during this measurement due to noise in atom number and the unknown overlap between the displaced MOT and probe laser. The MOT was not in the cavity and the probe beam waist (about 0.4 mm of diameter in the MOT) was different to that of the cavity mode. However, the position of the gain peak relative to other spectroscopy features does not depend on the atom number and that was the purpose of this measurement. Figure 5.4 shows the gain spectrum.

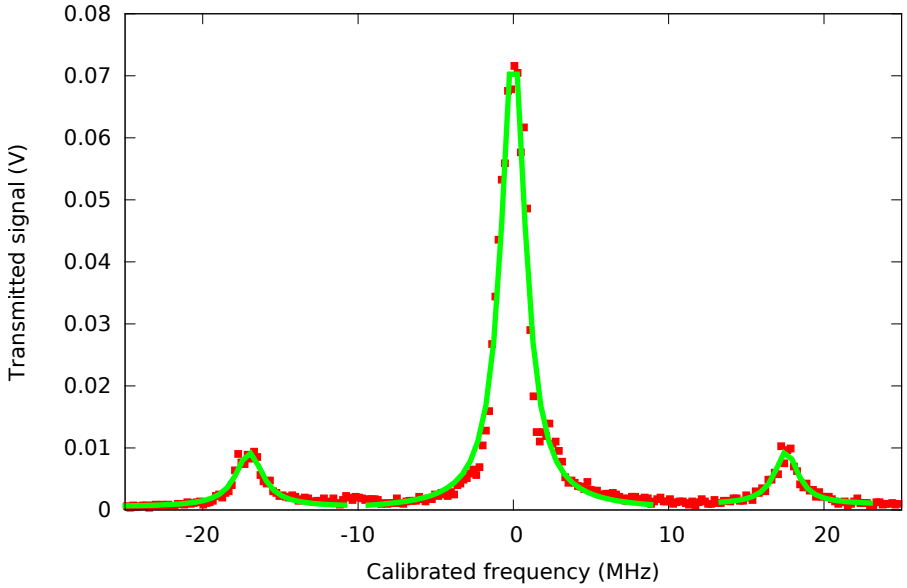

Figure 5.3 Cavity transmission for calibration of the gain measurement. The green lines show individually fitted Lorentzians. The side peaks show the frequency modulation at 17.288 MHz.

*Note that for the gain measurement the MOT was moved outside the ring cavity.

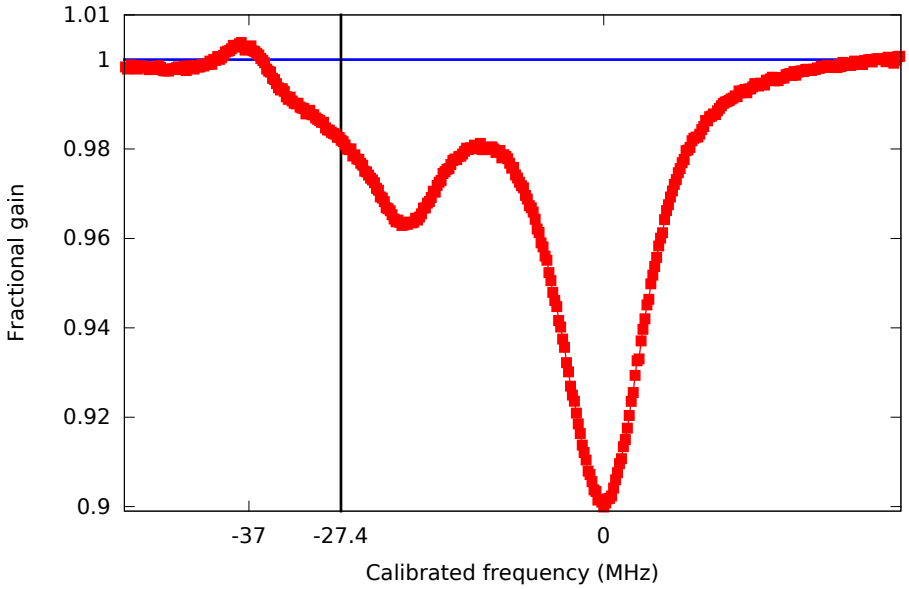

Figure 5.4 Gain peak near the $2 \rightarrow 2'$ (cooling) transition. The frequencies are relative to the Stark shifted $2 \rightarrow 3'$ transition (see Figure 3.6 for D_2 energy levels) and the third nearby transition $2 \rightarrow 1'$ is not strong enough to be seen in this measurement. The vertical black line shows the cooling frequency given by the beat note between the cooling and probe beams. The data should follow the blue line outside the gain/absorption features, but there was too much noise during the ramp.

Conclusion on Gain Measurement

This section showed experimental data on optical gain in the running ^{39}K MOT. The centre frequency of the gain peak, relative to the MOT cooling frequency, was further investigated in additional measurements.

An ideal probe beam would have the same size as the lasing mode (cavity mode). In this case, it was not possible as, owing to the big vacuum chamber, shimming coils, and the MOT beam optics, the nearest lens that could be in the path of the probe beam was already about half a meter away from the MOT. As a result, the probe beam diameter was estimated to be 0.4 mm in the MOT (around 4 times the cavity waist and half the FWHM size of the MOT).

In principle, the probe beam should be weak enough so it cannot disturb the gain medium, although the power had to be increased to distinguish the gain peak from the noise and make a decent measurement, thereby enhancing the height of the gain peak, but reducing the fractional gain.

Because of the different position of the MOT with respect to the MOT beams, the high probe power, its size compared to that of the MOT, and misalignment with respect to the cavity axis and the shape of the MOT, the measurement was only optimised to prove that there was gain and not necessarily to accurately quantify the amount of gain. The baseline (fractional gain) was too noisy (not a flat line) to determine the exact width and height of the gain peak. We can however conclude that the width was on the order of the cavity linewidth and the height was on the order of the round-trip cavity losses. Still, the data could be used to estimate the centre frequency (predicted by Equation (2.7)) and width (predicted by Equation (2.8)) of the gain peak in order to compare it to theories of different gain mechanisms (the centre frequency is the main information, but a Raman gain feature is much narrower than Mollow gain) [8] as seen in the next section.

5.1.2 Determining the Gain Mechanism

The gain mechanisms observed in a MOT depend on the pump frequency [8, 17, 18]. Our simple setup provided both the MOT beams and pump beams at once, which means that their frequency could not be changed separately. It was however still possible to move the gain peak by changing the cooling frequency without reducing the height of the gain peak too much due to decreasing the atom number. The gain peak could be moved far enough to track it with a theoretical prediction (Equation (2.8) and dotted curve in Figure 5.5) for the Mollow gain induced by the cooling beam scattering from

the $2 \rightarrow 2'$ transition. Since I had left the laboratory, there were slightly more accurate predictions involving more energy levels [43].

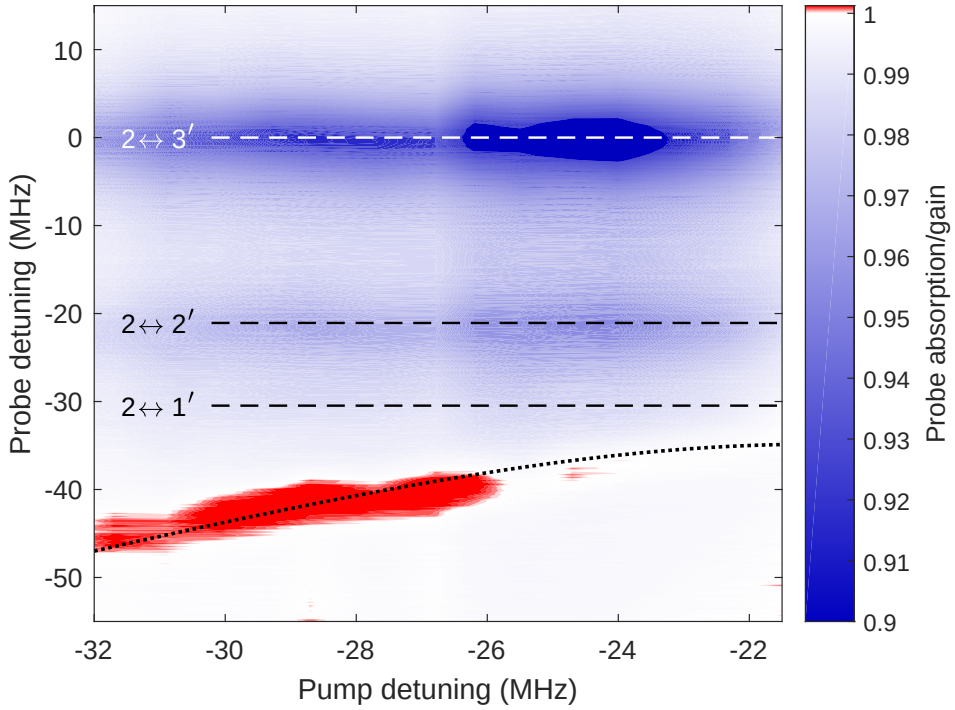

Figure 5.5 Gain peak as a function of MOT cooling detuning. The dashed black line shows the theory curve (see Equation (2.7) and [43]). The pump (cooling) detuning is relative to the $2 \rightarrow 3'$ (strongest) transition. -27 MHz is the normal detuning optimised for the highest atom number, but the centre frequency of the gain peak does not depend on atom number and the gain peak is resolvable as long as the atom number is not too low.

Conclusion on Gain Mechanisms

These measurements compared the theory for Mollow gain, to the detected gain peak varied as a function of pump frequency. The overlap suggested the dominant gain mechanism was indeed Mollow gain.

5.2 Transverse Patterns of Laser Outputs

5.2.1 Theory of Hermite-Gaussian Modes

In Section 2.3 the cavity field was only treated in one dimension, that is, the propagation axis z. In order to describe the transverse intensity distribution of TEM_{lm} modes, it is necessary to deal with the transverse coordinates (x and y) as well [24, 26, 46, 61, 62]. The solutions to the paraxial Helmholtz wave equation for a linearly polarised classical electric field amplitude treated as $\left|\vec{E}\right|(\dots) = E(\dots)$ are of the form

$$E_{lm}(x,y,z) = \mathcal{N} H_l\left(\frac{\sqrt{2}x}{w_x(z)}\right) H_m\left(\frac{\sqrt{2}y}{w_y(z)}\right) e^{\frac{x^2}{w_x^2(z)} - \frac{y^2}{w_y^2(z)}} e^{-ik\left(z + \frac{x^2}{R_x(z)} + \frac{-y^2}{R_y(z)}\right) + i\Phi_{G_{lm}}(z)}, \tag{5.1}$$

where $H_{\dots}(\dots)$ denotes the Hermite polynomials, $\mathcal{N}$ is the normalisation, $w_{x,y} \propto \sqrt{1 + \left(\frac{z}{z_{R_{x,y}}}\right)^2}$ are the waists along x or y, $R_{x,y}(z) = z\left(1 + \left(\frac{z_{R_{x,y}}}{z}\right)^2\right)$ are the wavefront radii along x or y, $z_{R_{x,y}}$ are the Rayleigh lengths in the $x-z$ or $y-z$ planes, and $\Phi_{G_{lm}}(z)$ is the Gouy phase shift.

Unlike Gaussian beams, the above Hermite-Gaussian beams match the curvature of spherical mirrors, which are also used in resonators. Substituting this solution into the paraxial Helmholtz equation and using the separation of variables, we end up with an eigenvalue problem that is solved by the Hermite polynomials [62].

TEM_{00} has one Gaussian intensity peak in the transverse plane, but higher-order modes have several ones as also measured in the experiment (Section 5.2.2). As the cavity waist of TEM_{00} is $5-7$ times smaller than the size of the MOT, higher-order transverse modes overlap with enough atoms to exceed their lasing threshold, according to what was observed.

5.2.2 Tranverse Patterns of Lasing Modes

Beam Profile Measurement

The first evidence of lasing is of course the fact that there is output light. In this setup, nothing restricted lasing to TEM_{00} as the cavity mirrors, pump beams (MOT beams), and the atom cloud were all big enough to sustain higher-order modes.

The fact that the laser output was continuous allowed for slower measurements as well. Both cavity modes (directions) could be observed on the same beam profiler CCD (Section 4.1). It was also used for power detection, but it had to be calibrated first. Figures 5.6 and 5.7 show lower- and higher-order modes, and Figure 5.8 is the calibration curve of the beam profiler. Unfortunately, the software rescaled the pictures, but this could be corrected for by comparing the numbers of pixels and ranges of interest of the calibration and other pictures. The system was too noisy (flickering MOT and strongly competing unstable transverse modes) to make slow measurements. The beam profiler software (Thorlabs) calculated the optical power so it was already calibrated, which was used for calibration of the saved pictures, but the the region of interest had to be reduced (to eliminate background noise and scattered MOT light) and the triggered pictures (milliseconds of exposure time for each picture) were rescaled and had no information on optical power any more. This was more of a software engineering issue than anything physical. With the calibration curve and the region of interest that was set for series of fast measurements, the optical power could be extracted afterwards as there was a relation between pixel counts, region of interest, and total optical power. However, these measurements show the rich variety of transverse modes. The TEM_{00} was sometimes only seen when the cooling

power was reduced a bit. The TEM_{11} was very close (this was true of the empty cavity spectrum as well [26]) and could not be excluded completely even for low atom numbers. Competing transverse modes were also reported in a ytterbium MOT with an extra pump field [20].

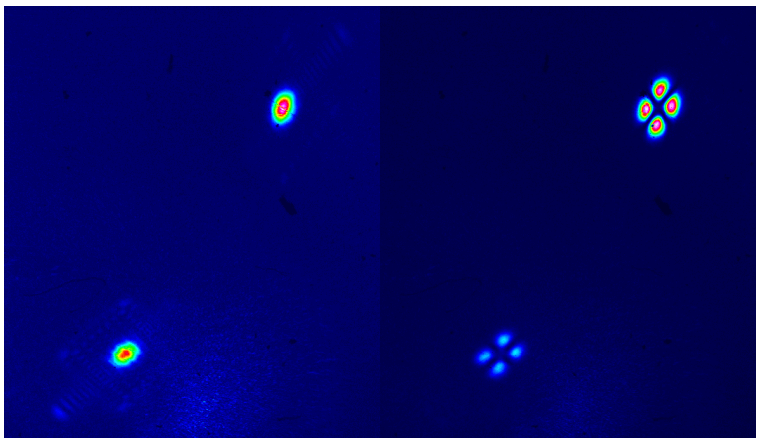

Figure 5.6 Rescaled false-colour pictures of counterpropagating TEM_{00} and TEM_{11} lasing modes. Top peak: CCW. Bottom peak: CW.

Figure 5.7 Rescaled pictures of the counterpropagating lasing modes with increasing power (original ROI area = 4024.80 µm × 4411.80 µm). The power shown in each picture corresponds to the total optical power.

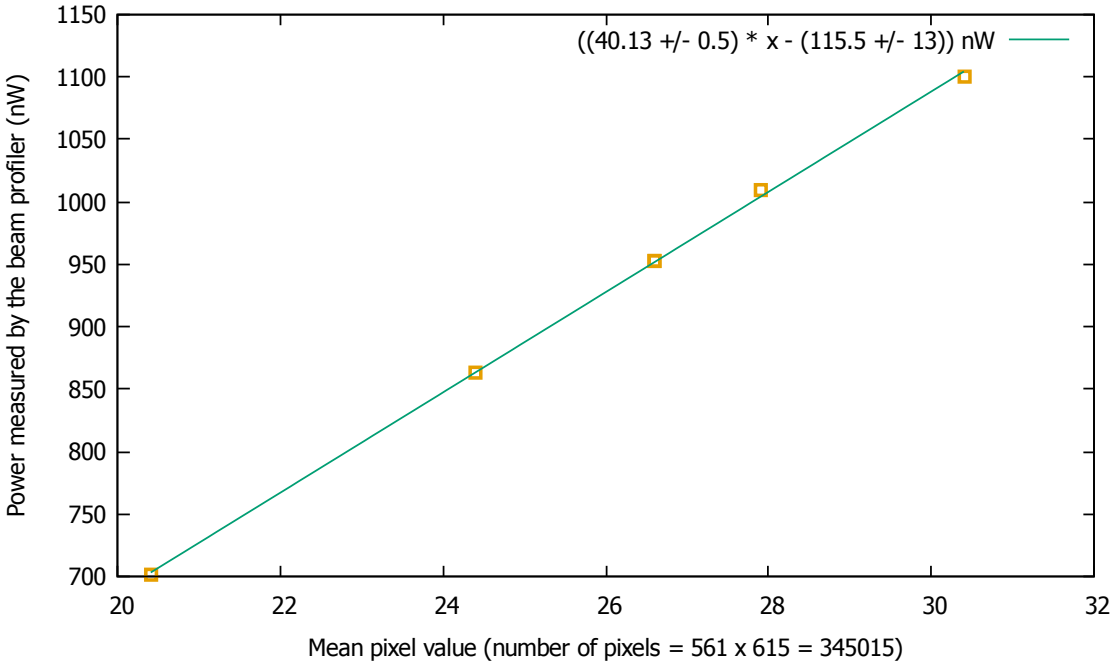

Figure 5.8 Beam profiler calibration based on Figure 5.7, knowing the total optical power for each picture.

Conclusion on Transverse Patterns

Some experiments apply a diaphragm or an aperture to increase the losses of higher-order modes, analogously to commercial lasers. Otherwise, it is not straightforward which modes will survive. Of course, the TEM_{00} is desired in applications. Higher-order modes have a larger overall waist, although the overlapping optical intensity and MOT density are generally lower when parts of the beam are farther from the geometric centre if we assume that the transverse modes have the same total power. The system was not stable enough to characterise this, but it was the balance between the larger waist, smaller intensity, and lower atomic density. The only conclusion which we can be confident about is that higher-order modes seemed to dominate for high atom number and pump (cooling) power. This was also observed in

other experiments (see [20], for example). In the measurements, the atom number and pump power (both affect gain) were chosen to mostly exclude higher-order modes as mentioned in the next sections.

5.3 Onset of Lasing and Second-Order Coherence $g^{(2)}$

Section 5.1.1 demonstrated the presence of optical gain in the atomic cloud and Section 5.2.2 showed the output intensity profile of the laser. This section will describe lasing in a more general way. Lasers are expected to have a threshold as the gain increases and a second-order coherence $g^{(2)}(\tau) \simeq 1$. The former is well-known and usually evident to measure, whereas the latter is more laborious and rarely done. The high-bandwidth detection that is necessary for $g^{(2)}(\tau)$ also helps gain some insight into short timescales and gives further information when it is done to both lasing outputs at the same time (see Section 5.4.2).

5.3.1 Threshold Measurement

The cavity was locked to TEM_{00} CW and CCW modes, the push beam that creates the atomic beam loading the MOT was turned off, turned back on again when there was no 3D MOT, and pictures of the MOT and the cavity outputs were taken while the 3D MOT was being loaded (Figure 5.9).

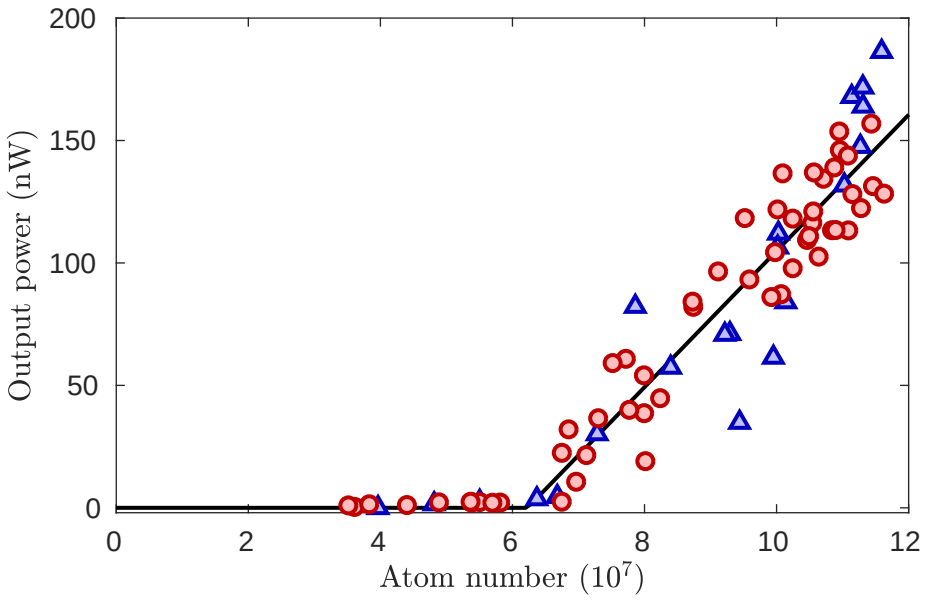

Figure 5.9 Laser threshold curve as a function of the total atom number in the MOT. Red curves: CW. blue triangles: CCW. The solid black line is a fit with the slope of 2.8 fW/atom and the threshold atom number of 6.2×10^7.

5.3.2 Theory of Second-Order Coherence

Definition of Second-Order Coherence

The second-order coherence was first used for determining the size of an object [63] through the spatial coherence, but it can also give information on the type of light source [28]. Only the time delay was varied in the experiment and it was applied so as to gain evidence of lasing, since lasing and fluorescence show different intensity correlations, which will be explained in this theory section. The second-order coherence is defined as

$$g^{(2)}(\tau) = \frac{\left\langle \hat{E}^{(-)}(t)\hat{E}^{(-)}(t+\tau)\hat{E}^{(+)}(t+\tau)\hat{E}^{(+)}(t) \right\rangle}{\left\langle \hat{E}^{(-)}(t)\hat{E}^{(+)}(t) \right\rangle \left\langle \hat{E}^{(-)}(t+\tau)\hat{E}^{(+)}(t+\tau) \right\rangle}, \tag{5.2}$$

where $\hat{E}^{(\pm)}(\dots)$ is the electric field operator and the $\pm$ denotes the positive/negative frequency parts of the field. The spatial coordinates are omit-

ted, because the fields come from the same source and only the time delay is varied. $g^{(2)}(\tau)$ can be rewritten in terms of intensity $I(t)$:

$$g^{(2)}(\tau) = \frac{\langle I(t)I(t+\tau)\rangle}{\langle I\rangle^2}, \tag{5.3}$$

which assumes that mean intensity is constant.

$g^{(2)}$ of Laser

It is well known that a monochromatic coherent field (e.g. the output of a laser) has Poissonian statistics as [38]

$$g^{(2)}(\tau) = g^{(2)}(0) = 1. \tag{5.4}$$

$g^{(2)}$ of Fluorescence from Single Two-Level Atom

It can also be shown that light scattered from a single two-level atom shows antibunching and sub-Poissonian statistics [38, 64], that is,

$$g^{(2)}(\tau) \geq g^{(2)}(0) < 1. \tag{5.5}$$

This can be proved by substituting the atomic raising ($\sigma^\dagger = |e\rangle\langle g|$ - meaning **e**xcited and **g**round states) and lowering ($\sigma = |g\rangle\langle e|$) operators multiplied by the appropriate constant into the dipole operator in the radiation electric field of an oscillating dipole. In Equation (5.2) we can now write

$$g^{(2)}(0) = \frac{1}{\langle\dots\rangle\langle\dots\rangle}\left\langle \underbrace{\sigma^\dagger(t)\ \ \sigma^\dagger(t+0)}_{(\sigma^\dagger)^2=0}\ \ \underbrace{\sigma(t+0)\ \ \sigma(t)}_{\sigma^2=0}\right\rangle = 0, \tag{5.6}$$

since the atomic operators cannot be applied twice.

$g^{(2)}$ of Fluorescence from Many Two-Level Atoms

Even though it is experimentally easier to measure fluorescence from many atoms, the theory is rather complicated and less obvious. In the literature there are some analytical formulas for atoms without a cavity [65–67], which give some intuition. Transition between one-atom and many-atom fluorescence has also been demonstrated experimentally [64]. For many atoms, the result is bunching and super-Poissonian statistics:

$$1 \leq g^{(2)}(\tau) < g^{(2)}(0), \tag{5.7}$$

and the short explanation is that atoms emit photons independently and when they interfere constructively, more photons are likely to be registered after detection of one photon, which represents super-Poissonian statistics.

Analysis of $g^{(2)}$ Data

If the field is detected by two detectors in different locations, Equation (5.3) can be rewritten in terms of photon counts (proportional to intensity) n_1 and n_2 detected on the two detectors:

$$g^{(2)}(\tau) = \frac{\langle n_1(t) n_2(t+\tau) \rangle}{\langle n_1(t) \rangle \langle n_2(t+\tau) \rangle}. \tag{5.8}$$

The numerator is the average of coincidences. In practice, it takes some time to detect and register photon counts, and therefore it is more precise to say $n_{1,2}(t)$ are the numbers of counts on channels 1 or 2, detected within times t and $t + \Delta\tau$. Since photon counters emit square pulse signals that are then timestamped, $n_{1,2}$ are the histogrammed timestamps. Ideally, t runs through a sample that has a constant mean count rate. $g^{(2)}(\tau)$ is the

appropriately normalised cross-correlation function of vectors $n_{1,2}$ that have the length of the sample duration divided by $\Delta\tau$. If the bin size $\Delta\tau$ is not much larger than the timescale given by the maximum count rate of the detectors, most time bins contain zero counts. In this case, $g^{(2)}(\tau)$ functions calculated from many samples have to be averaged.

An equivalent way is to calculate the histogram of the time differences of the timestamps on the two channels and normalise it correctly.

The same result can also be achieved with only one detector, except that $g^{(2)}(0) = 1$, that is, for the very first $\Delta\tau$-sized bin when $n_1(t) = n_2(t)$ for all t, but it is correct for $\tau > 0$.

5.3.3 $g^{(2)}$ Measurement

This measurement used the Hanbury Brown-Twiss setup shown in Figure 5.10 [63].

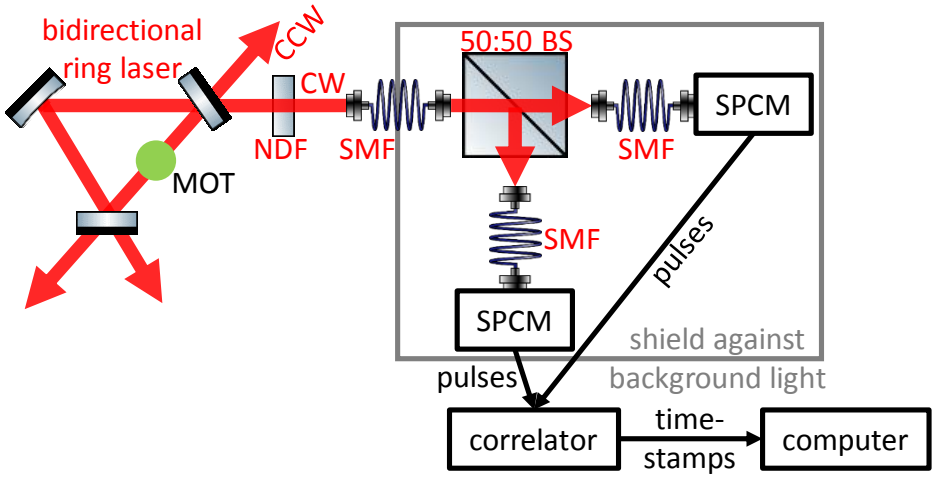

Figure 5.10 Simplified schematic of the $g^{(2)}$ measurement. NDF: neutral density filter, BS: beam splitter, SMF: single-mode optical fibre patch cord and couplers, SPCM: single photon counting module. Black paper and tapes were used to eliminate the background light.

Anything that measures intensity could be used, but the bandwidth of

the detector limits the time resolution of $g^{(2)}(\tau)$. For this purpose, single photon counting modules (SPCM) are commonly used.

The MOT was running continuously, the cavity was locked to the TEM_{00} CW mode, which was attenuated by neutral density filters and coupled into a single-mode fibre connected to a Hanbury Brown–Twiss setup (Figure 5.10) with two identical SPCMs.

For fluorescence, the atom number was decreased (around 4×10^7) just below the threshold of lasing by attenuating the MOT beams. The cavity was locked to the biggest fluorescence peak observed in one direction with an SPCM. The correlator sent timestamps in units of 81 ps. About $10^6 - 10^7$ counts were analysed with 5 ns resolution. In the fluorescence measurement, there were no attenuators between the cavity and the fibre (the count rate was $10^3 - 10^4$). When the lasing output (with an atom number of about 8×10^7) was measured, an attenuation of about 10^4 was used to protect the photon counters. The atom number was hard to control for the minimum averaging time, but it was above lasing threshold most of the time. Fluorescence had a different frequency (Figure 5.4) and cavity length so the two measurements also had to be made at different cavity lengths (when it was lasing, only the TEM_{00} was sufficiently coupled into the fibre, even though it was lasing at all cavity lengths).

The data are plotted in Figure 5.11. Lasing shows a flat curve $\simeq 1$ as expected. It is slightly above 1, which is attributed to the presence of small amounts of higher-order transverse modes in the single-mode fibre. Fluorescence has a time constant of about 170 ns. This timescale is higher than both the atomic and cavity decay rates. There is not a straightforward analytical way to explain it, but for our parameters cavity-decay simulations (see supplements in [43]) done after my departure were in agreement with

the measurement.

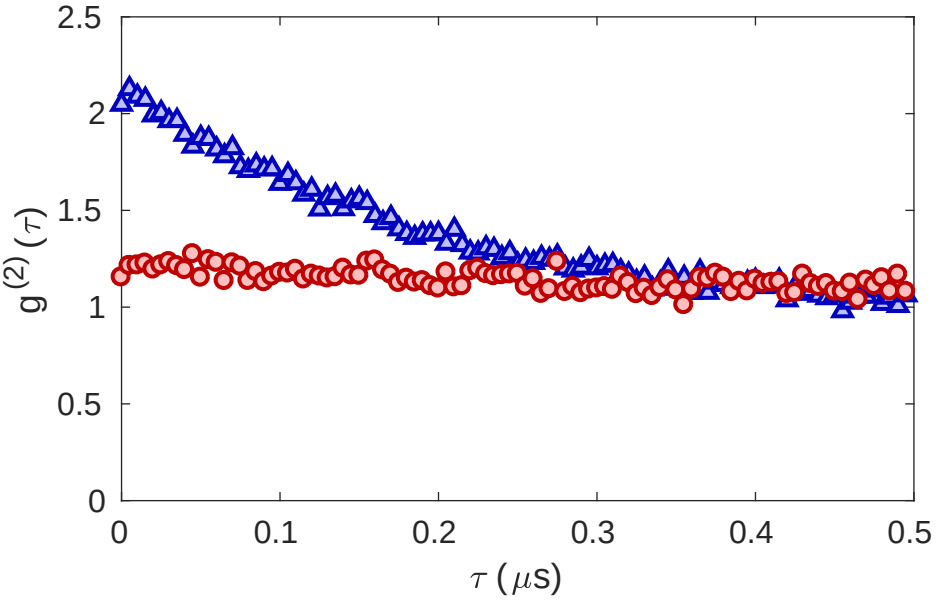

Figure 5.11 $g^{(2)}(\tau)$ data. Blue: $g^{(2)}(\tau)$ of fluorescence and red: $g^{(2)}(\tau)$ of lasing.

Conclusion on Threshold and $g^{(2)}$

As a function of total MOT atom number, a lasing threshold was observed in both counterpropagating cavity directions. Further evidence of lasing was gained by distinguishing fluorescence (occurring below the threshold atom number) from lasing, the latter showing an output power orders of magnitude higher than fluorescence. Fluorescence was super-Poissonian and lasing had a flat $g^{(2)}(\tau) \simeq 1$ as confirmed by the measurement.

It is important to emphasise that fluorescence below threshold had a different frequency and was measured at a different cavity length. This means that during the data acquisition there was not a continuous transition between fluorescence and lasing, and separate measurements had to be made. Fluorescence light only came from the MOT beams. The biggest peak as a function of cavity length was assumed to be the TEM_{00} mode at the cooling

frequency as the repump was significantly weaker, and both beams were in the same place and had the same alignment.

In addition to the previous data, one could measure an intensity threshold as a function of pump power, and a transition in $g^{(2)}$ as a function of atom number or pump power. In principle, the Rabi splitting could tell the in-cavity atom number. After some attempts, these ideas did not prove to be feasible due to noise in the MOT beam intensity and atom number. Averaging did not help obtain clean data of these measurements either. However, the existing data still proved that the system behaved as a laser.

5.4 Counterpropagating Lasing Modes and Nonreciprocity

5.4.1 CW and CCW Spectra

The cavity length was moved close to the two TEM_{00} outputs while looking at the beam profiler. Both outputs were coupled into a single-mode fibre connected to two identical avalanche photodiodes (APD). The same APD was used when the cavity was probed as described in earlier works [26, 27, 58], but in this case there was no probe beam, the cavity was scanned, and both counterpropagating directions were measured (Figure 5.12). Equations (2.35) and (2.38) explain the parabola shape, since Equation (2.38) describes a linear dependence of the lasing frequency on the empty cavity resonance frequency and Equation (2.35) shows a quadratic dependence on the lasing frequency. The cavity was scanned across the TEM_{00} peaks and parabolas were fitted to 66 spectra (Figure 5.13). Each spectrum was an average of 4 traces on the oscilloscope. The inferred average frequency nonreciprocity (splitting between the two counterpropagating modes) is about

2 MHz, although it is only a rough approximation as it does not take into account the phase shift caused by the gain medium. It was calculated in two steps. The cavity piezo voltage was converted to frequency, using the PDH sidebands in the empty cavity. Then the theory for the empty cavity (round-trip condition for different cavity lengths) was used for converting frequency to length. The reason for the conversion is that the change in cavity length would not easily be understandable without knowing the parameters of the cavity and putting them in the formulas.

The theory and causes of CW/CCW splitting in cavity length are currently under investigation.

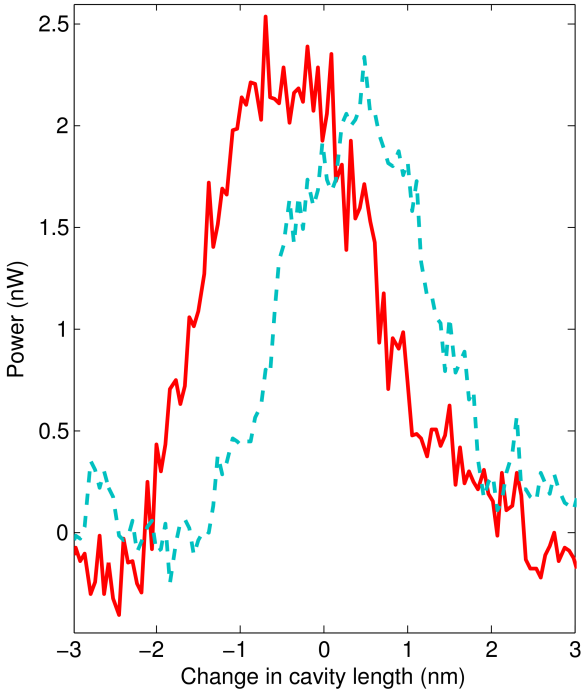

Figure 5.12 Cavity output spectrum around the TEM_{00} peaks in both directions. Red and dashed blue curves show CW and CCW directions, respectively.

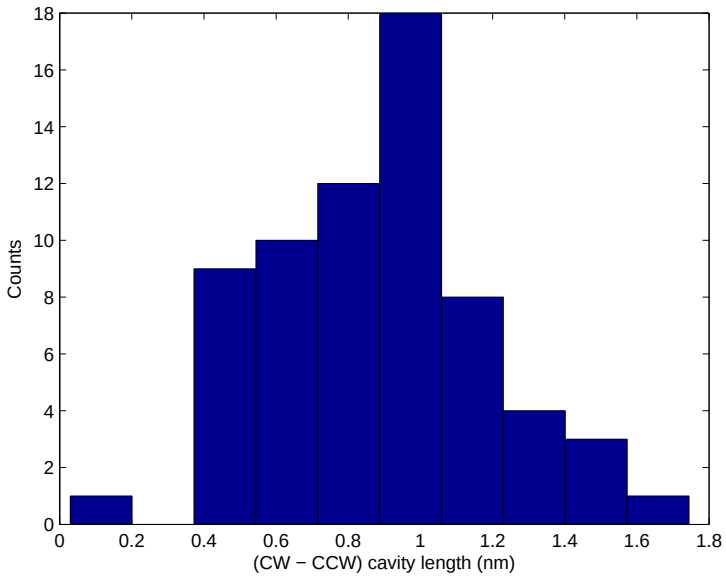

Figure 5.13 Histogram of the difference between the position of the counterpropagating TEM_{00} peaks, in cavity length.

The cavity ramp time had to be at least a few ms to keep it linear and the APDs had a bandwidth of 3 MHz. However, in the next section we will see that lasing stopped being simultaneous on short timescales.

5.4.2 Cross-correlation

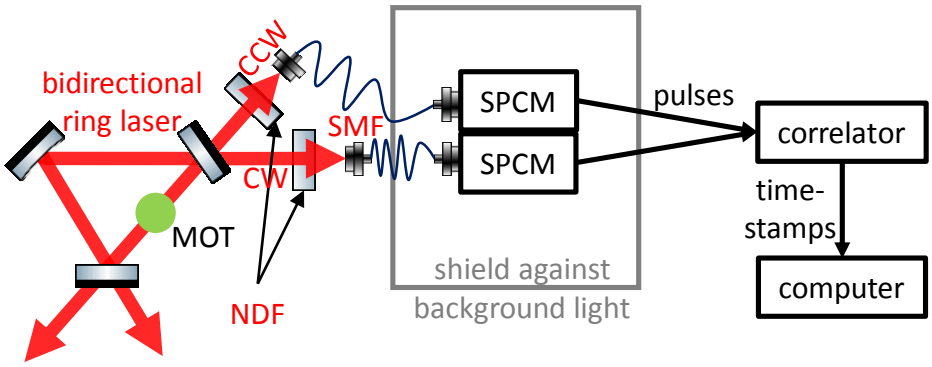

Figure 5.14 Simplified schematic of the cross-correlation measurement. NDF: neutral density filter, SMF: single-mode optical fibre patch cord and couplers, and SPCM: single photon counting module.

With SPCMs, both directions could be observed with good time resolution (Figure 5.14). Both cavity outputs were attenuated, coupled into a fibre, and connected to a SPCM. The competition for gain is clear in Figure 5.15. The counts were histogrammed into 60 µs bins. The cross-correlation is defined by

$$g_{12}^{(2)}(\tau) = \frac{\langle n_{\mathrm{CW}}(t)\; n_{\mathrm{CCW}}(t+\tau)\rangle}{\langle n_{\mathrm{CW}}(t)\rangle\,\langle n_{\mathrm{CCW}}(t+\tau)\rangle}, \tag{5.9}$$

where $n_{(\mathrm{C})\mathrm{CW}}$ denotes the detected counts for each cavity mode and, as opposed to the $g^{(2)}(\tau)$ measurement, the two outputs of the cavity were used instead of the outputs of the 50:50 BS, which was left out this time. 1 means no correlation and 0 means anticorrelation. In agreement with Figure 5.15 (very little overlap between the CW/CCW modes), the cross-correlation (Figure 5.16) went down to 0.042 for small τ. The resolution of τ was 10 µs.

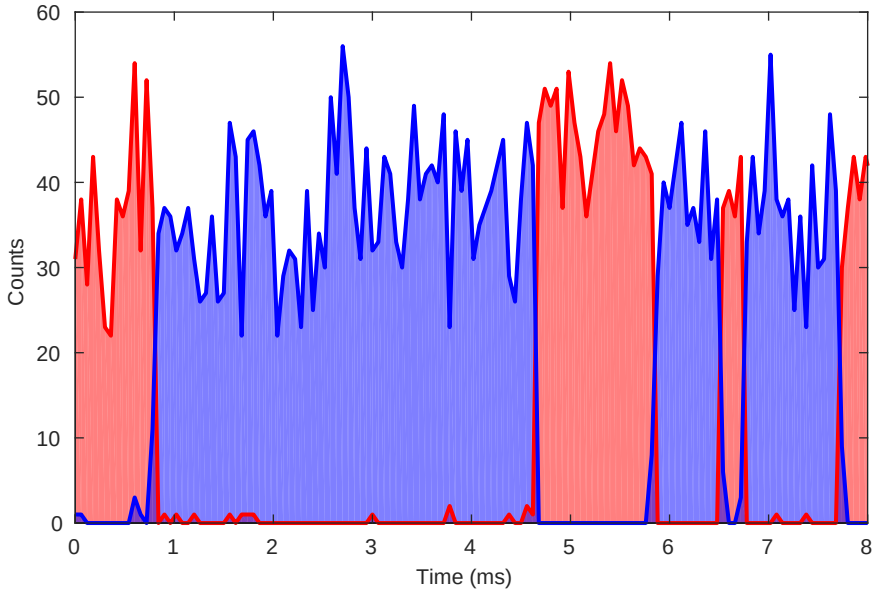

Figure 5.15 Competition between the two directions. Red: CCW and blue: CW. The counts were integrated over 60 μs intervals.

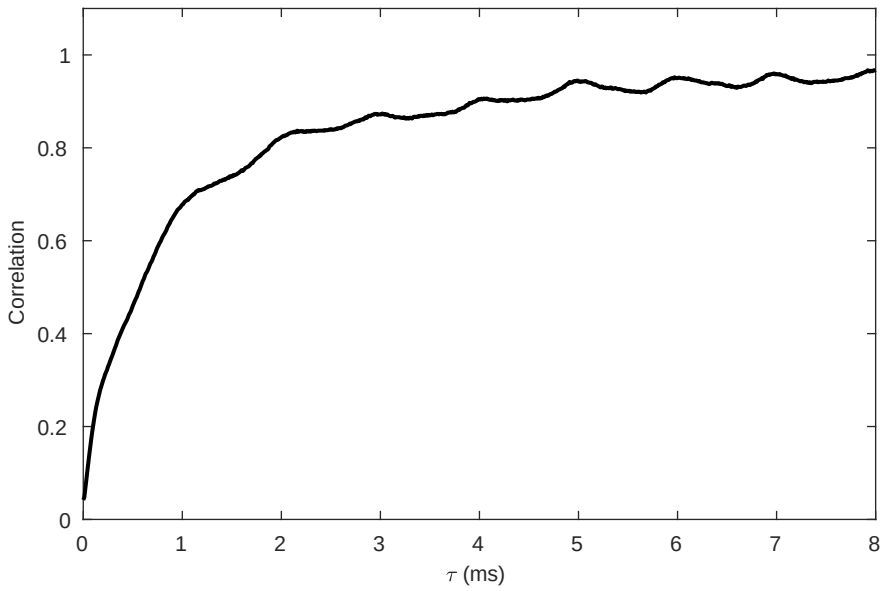

Figure 5.16 Cross-correlation of the counterpropagating laser modes.

5.5 Conclusion on Bidirectional Lasing

This chapter started with a ^{39}K MOT and a triangular ring cavity. When these two aligned and optimised properly, they work as a bidirectional ring laser. Experimental data on Mollow gain, output transverse modes, threshold, second-order coherence, and cross-correlation between the two counterpropagating lasing directions were shown.

Unfortunately, it was not possible to directly compare the frequency of the lasing modes to a reference, due to lack of time, suitable detectors, and/or alignment. Such a measurement could compare the CW and CCW modes. Gyroscopes also rely on this information (see Section 6.3). No conclusion has been reached so far on the exact causes of nonreciprocity between the two counterpropagating lasing modes, but at the time of writing, is being investigated. New measurements seem to agree very well with empirical models that describe bistability and the combined effects of magnetic field and beam alignment. Inhomogeneous magnetic field from the MOT coils, Zeeman shifts, or symmetry breaking owing to intensity-dependent lensing (Kerr effect) could contribute to nonreciprocal phenomena. Homogeneous gain media forbid simultaneous (CW and CCW) lasing [4], but different gain mechanisms that have directional dependence could make it possible to measure the frequencies of both modes at the same time without any added delays or reference beams.

To sum up, the experiment was set up to prove that cold atoms could serve as the gain medium of a bidirectional ring laser. The MOT beams and magnetic field were not changed or switched off while lasing, which, except for pulsing and switching on very short timescales, provided continuous lasing outputs. This made it relatively easy to set up, align, and optimise all

the measurements, since lasing was already observed without any experimental shots, cycles, delays, or loading times. Based on the data and the experience that was gained, the same (and more) measurements could be made with different gain mechanisms as well (see Chapter 6).

Chapter 6

Outlook

The main chapters of this thesis summarised the inevitable changes to the vacuum system, laser system, and the optimisation and measurement procedures for the higher atom number, better atom-cavity alignment, and bidirectional lasing. The next big steps in the experiment will be likely to follow a similar pattern: optimisation of the MOT, improvements in the alignment, and new measurements. The main goal is to separately pump the two counterpropagating directions. Mollow gain does not have any directional dependence, whereas four-wave mixing does [31].

The MOT coils have never been switched off during measurements, even though part of the problem should now be solved (see vibration isolation in Sections 3.1.1 and 4.1.1). However, switching off the coils would not switch off the background field (the Earth's field and contribution of other things, for example, the optical table). Six shimming coils were set up to provide a uniform magnetic field along three Cartesian axes. They were only applied to adjust the position of the MOT. Once optimised, these coils can then be called compensation coils, and allow for zero magnetic field, and therefore no Zeeman shifts. This is essential to optical molasses, efficient sub-Doppler

cooling (for narrower transitions [27]), narrow dispersive features, and frequently used in precision measurements with trapped atoms.

There are other gain mechanisms (Section 6.1) that are more beneficial, also because they can be optimised separately to the MOT beams. In addition, far-off resonant pump beams result in larger coherence times, and the two counterpropagating cavity modes can be pumped independently with four-wave mixing, which means simultaneous lasing, so that the beat note can be detected directly without any artificial delays or reference beams.

The bidirectional spectrum was measured as a function of cavity length, but (as explained in Section 2.3.2) that is not equivalent to frequency. In active sensing applications (Sections 6.2 and 6.3) the main information is the frequency of the lasing modes. Unfortunately, this was not yet achievable, but a better detector or more lasing power from different gain mechanisms should make it easier to overcome this technical issue. The source of nonreciprocity is also yet to be investigated.

6.1 Raman Gain and Four-Wave Mixing

Raman gain and four-wave mixing have also been used for cold atom lasers [17, 18]. Raman scattering is a two-photon transition between dipole forbidden transitions (e.g. hyperfine ground states) [31]. The same pump beam can provide both Mollow gain and Raman gain at different frequencies and the cavity length can switch between the two mechanisms (see [8] for theory formulas), although the pump beam is usually far detuned (by hundreds of MHz). In our ^{39}K experiment, the level structure is different (absorption peaks can destroy the gain features), but after I had left the lab, informal discussions revealed that it was indeed possible to see Raman gain in this species as well with the right pump detuning and power.

Four-wave mixing [17, 31, 68, 69] is a third-order nonlinear process involving two pump fields with the same or different frequencies and could separately pump the CW and CCW cavity modes because of its directional dependence [31], eliminating the issue with simultaneous lasing as homogeneously broadened media in ring lasers generally provide bistable outputs [4], but the two directions could also be pumped separately. Four-wave mixing offers both slow light and fast light [68], has already been demonstrated in a ^{87}Rb vapour cell (similar level structure), and the pulling effect was characterised [69]. An overview of the level schematic is shown in Figure 6.2. In our experiment, it would require an additional pump beam on the D_1 line, which was never been tried during my time, although the laser that was used for probing the MOT and measuring gain could be tuned to D_1 as it is only a few nm away in ^{39}K. [17] describes a system that can provide all the three gain mechanisms in a linear cavity by changing detunings and switching off either of the pump beams.

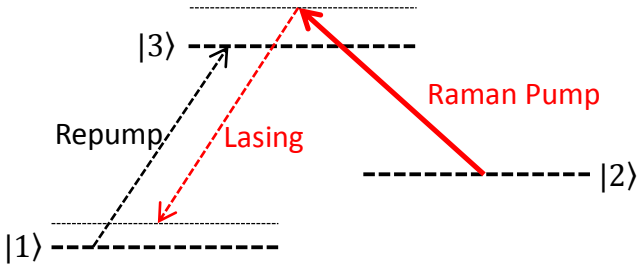

Figure 6.1 Raman gain uses the same type of configuration as Mollow gain. [18] describes this Raman gain scheme in an operating ^{87}Rb MOT (similar level structure to ^{39}K).

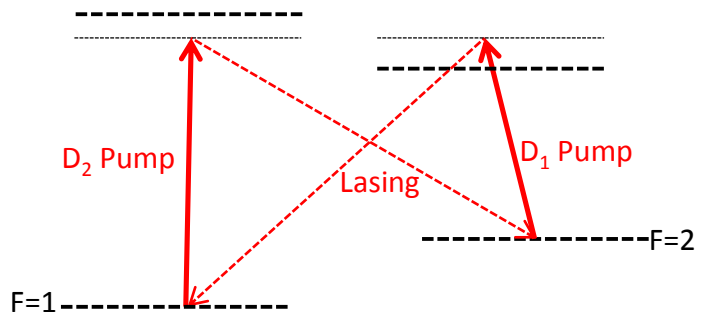

Figure 6.2 This configuration provides lasing when a cavity is tuned to either of the two lasing fields. The pump fields are tuned close to the D_1 and D_2 hyperfine levels. This scheme was used in [69].

6.2 Active Clock

An active clock [10] is a laser whose frequency depends on the gain medium instead of the cavity used for feedback (as opposed to conventional lasers, which are tuneable by their cavity) as it is meant to be a stable reference. The cavity can be made broader than the gain medium, which is called a bad cavity or white-light cavity [70]. The second approach is to make the gain medium very narrow by using dispersion, which also affects the lasing frequency (Equation (2.38)). Mollow gain would be suitable for this as slow light (a single gain peak provides slow light) gives a high group index, which eliminates the Sagnac effect. However, it would not be the best choice for this as it has a gain width similar to our cavity linewidth. Raman gain would be better (see, for example, [71] for demonstration in a vapour cell) as it has a narrower gain width [8] and was also seen in our experiment after my departure.

Active clocks can also be done in a linear cavity. A very high and narrow gain peak is desirable so as to increase the group index. If the corresponding atomic transition depends on the magnetic field, then it is a magnetometer.

Because gain is equivalent to slow light (assuming the gain bandwidth is less than the cavity bandwidth) if there are no additional dispersive features, it only requires a linear cavity, and can be tested without rotating it, an active clock is an easier task than a gyroscope and is already under development in other experiments [11–15].

6.3 Gyroscope

Although the current vacuum system cannot be rotated as it is rigidly attached and aligned to the optical table, cavity and MOT optics, the limits to how steep anomalous dispersion, which means small or negative group index, can still be investigated.

In terms of the experimental setup there is not much difference between slow light or fast light lasers. Gain media inherently give slow light, but the pump beam can be split into two nearby frequencies (Figure 6.3). This was demonstrated in [72]. Since most gain mechanisms depend on the detuning of pump beams, the two pump beams give two nearby gain peaks, which creates a dip. A dip in the gain peak is analogous to an absorption peak without actual absorption and corresponds to anomalous dispersion, that is, fast light, which is ideal for a gyroscope.

A proper frequency measurement of the lasing output could already answer the question whether the lasing frequency depends on the gain medium or the length of the cavity, which is also a way to characterise dispersion and, to some extent, sensitivity of the proposed gyroscope.

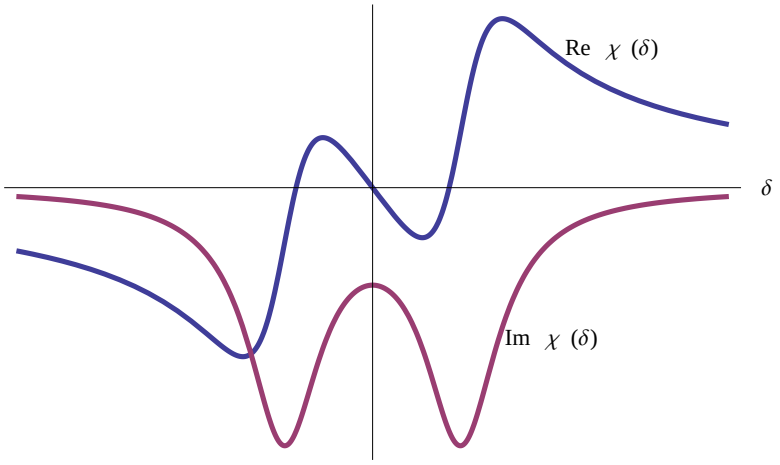

Figure 6.3 The sign of dispersion can be flipped. As explained in Section 2.1.1, $\mathrm{Im}(\chi) < 0$ means positive gain.

Appendix A

Stimulated Brillouin Scattering

While the main experiment was being upgraded, another kind of ring laser that supports both slow light and fast light was studied.

A.1 Theory of Stimulated Brillouin Scattering

Brillouin scattering is scattering from moving density fluctuations [31]. Stimulated Brillouin scattering (SBS) refers to scattering of a pump light from density fluctuations that move towards the pump in such a way that the interference of the pump and scattered light results in more fluctuations that further amplify the process. Density and intensity fluctuations can interact through electrostriction or heating caused by absorption. The latter is not desirable as the pump beam is meant to feed the lasing mode. Electrostriction is compression of materials caused by the electric field. It is a third-order nonlinear process. Both phonons and photons have a wave equation. The electrostrictive constant gives another relation between the

force phonons experience and the electric field. Without assumptions (e.g. constant pump intensity), these equations cannot be solved analytically in the time domain.

Only a very intense pump beam can induce sufficient fluctuations. Therefore, it is usually done in optical fibres, which have a small cross-section, increasing the intensity. Although fibres have a finite numerical aperture, to a good approximation, the whole process can be understood in one dimension.

A.2 Experimental Setup

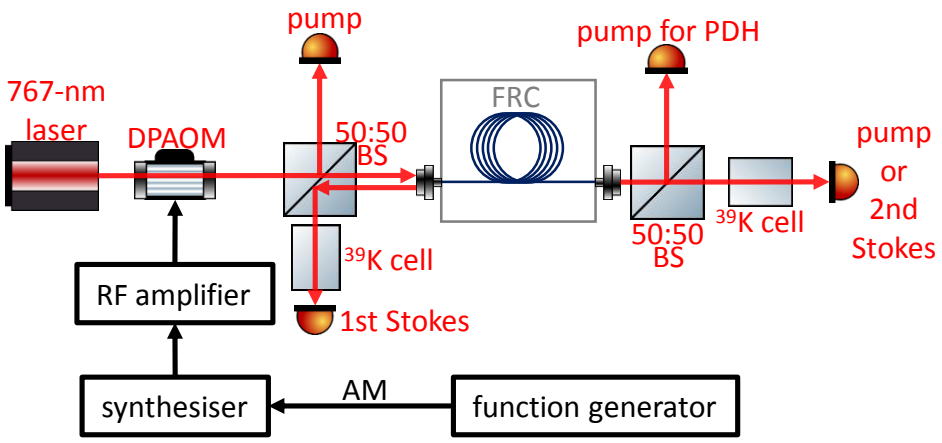

Figure A.1 Simplified schematic of the SBS experiment. DPAOM: double-pass acousto-optical modulator, BS: beam splitter, FRC: fibre ring cavity, PDH: Pound-Drever-Hall frequency stabilisation, and AM: amplitude modulation.

The experiment is illustrated in Figure A.1. As explained in Section A.1, the threshold in input optical power is very high in a few-metre-long silica fibre. The power build-up in the cavity lowers the minimum incident power, but, unfortunately, the optical elements absorb a significant amount of power. This necessitates a high-power laser*. The laser output was modulated by

*A Quantel EYLSA 767 was used.

an electro-optical modulator (not shown) for the laser to be locked to the cavity. The fibre-ring cavity comprised a tuneable evanescent directional coupler* and a polarisation-maintaining single-mode bare fibre, which was in a glass box that was in a metal box. The metal box was placed on sorbothane legs and covered with foam. These significantly reduced the noise in the resonance spectrum of the fibre cavity. Although no frequency reference was used in this setup, the laser was tuned close to a Doppler-broadened potassium† absorption resonance dip and locked to the nearest cavity resonance, which did not drift too far from the absorption dip during the measurements. At this point, the heated vapour cells absorbed the resonant light but were transparent at the red-shifted Stokes frequencies (see Section A.1). Otherwise the resonant light would have suppressed the much weaker Stokes beams. However, below the second threshold some pump light could still be measured after the cavity and vapour cell but became negligible compared to the second Stokes light when its threshold was reached.

Given how important the ring cavity is in the main experiment, it is important to note that this fibre-ring cavity behaves differently to the ring cavity described in Section 4.1, in that there is no reflection and transmission in the traditional sense. A small fraction of the input power enters the fibre cavity but most of it exits straight through the output A.2. The power in the cavity mode and the output power can still be given as a function of input power and the parameters of the coupler [73]. Unlike the usual cavity spectrum, near the maximum of the circulating in-cavity power there are only transmission dips (in our case, about $30 - 50\%$ deep) and no peaks.

*Evanescent Optics Inc.

†The atomic species had no role in this experiment and could have been done with different laser and vapour cell combinations (e.g. a rubidium laser and a rubidium vapour cell), although 1500 nm is usually the preferred wavelength in SBS experiments.

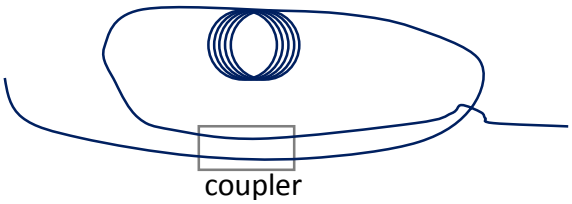

Figure A.2 Simplified schematic of the evanescent coupler.

A.3 Threshold

The backscattered power was characterised as a function of input pump power (Figure A.3). The threshold was around 5 mW. When the backscattered SBS became strong enough, it also started to act as a pump beam, and this process could repeat.

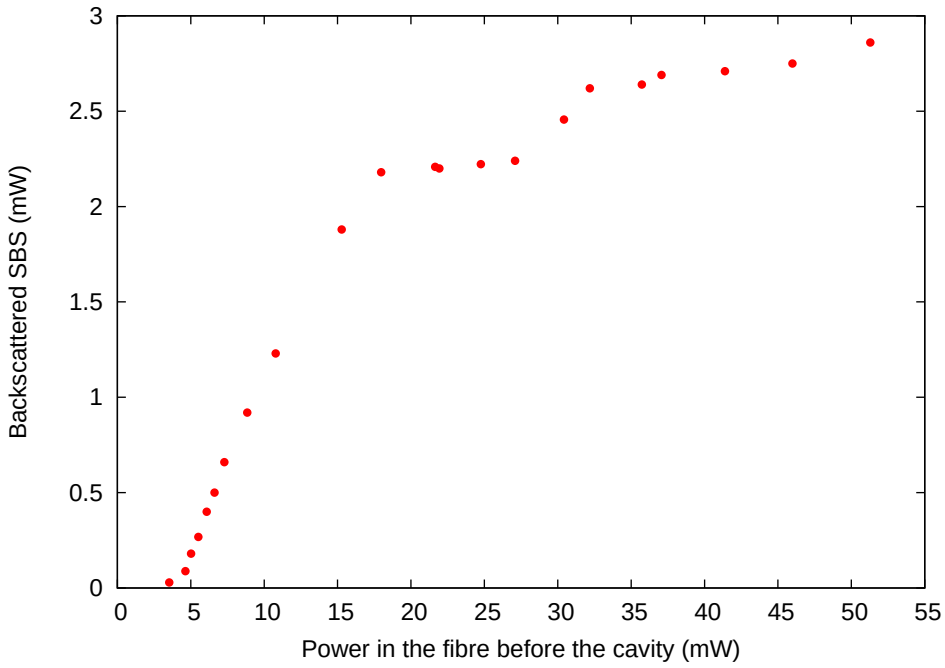

Figure A.3 A cascade of thresholds was measured as a function of input power to the fibre ring cavity.

A.4 Pulse Advancement

As the pump power was increased, it experienced more attenuation, which corresponds to anomalous dispersion. The backscattered SBS light saw a gain peak (slow light) and the pump beam saw losses (fast light). It is not equivalent to a simple absorptive medium as the pump is only absorbed when there is SBS light and there is no SBS light without the pump, and therefore there always has to be some pump light. Gaussian amplitude modulation (pulses) was sent to the AOM (Figure A.1). The pulses were detected before and after the fibre cavity (Figure A.4). Although, in general, the cavity acts as a slow light medium (meaning positive group index, positive delay,

and negative advancement), the pumping mechanism can be strong enough and still cross $n_g = 0$ (using the notation from Chapter 2). The most anomalous data were the following: $\tau_g = -3$ µs, $n_g = -180$, and $v_g = -1.7 \times 10^6 \ \frac{\text{m}}{\text{s}}$. Some of the oscillation and distortion around the output pulse were attributed to the noise overlapping the frequency spectrum of the Gaussian pulse.

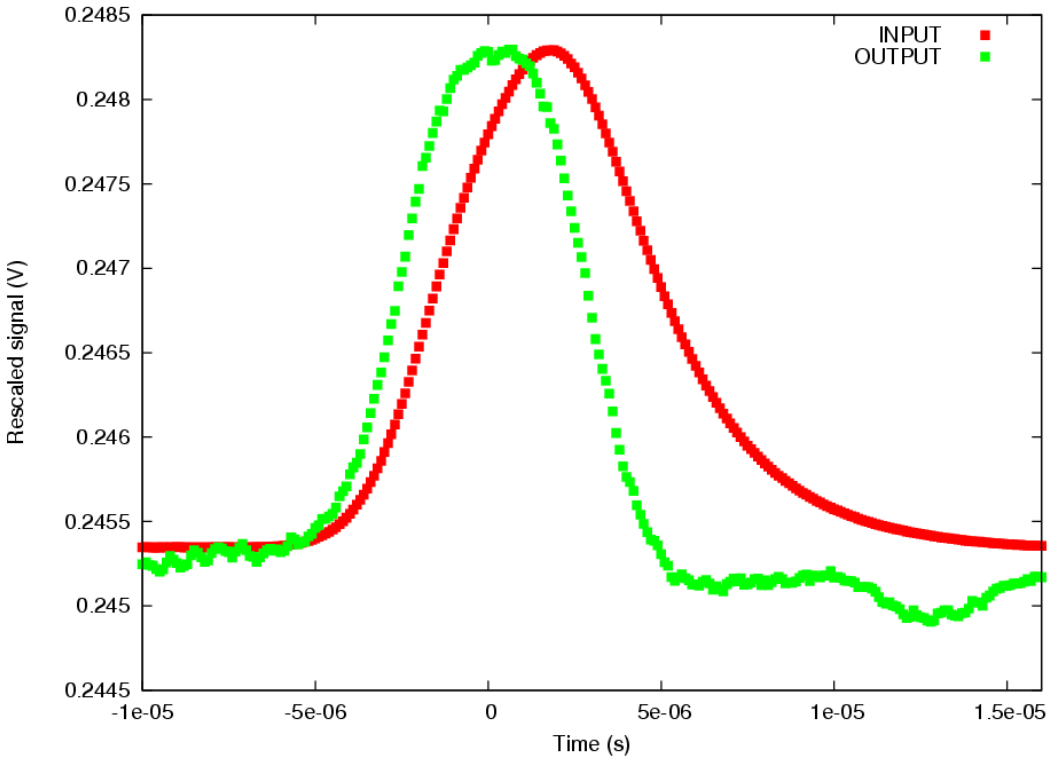

Figure A.4 Advancement of the pump beam. The pulse was detected before (input) and after (output) the cavity. The peak of the pulse had already left the cavity before it even entered the cavity.

List of Figures

2.1 Slow light and fast light during absorption and gain. The susceptibility and the group index are shown against the detuning. Similar curves can be found in [34]. 10

2.2 Dressed states of the coupled atom-light system. $|g\rangle$ and $|e\rangle$: ground and excited states of the non-interacting two-level atom, ω: the pump laser frequency, Ω: pump laser Rabi frequency, $|+,n\rangle$ and $|-,n\rangle$: eigenstates of the atom-light system with n photons, and $\tilde{\Omega}$: generalised Rabi frequency. . . . 11

2.3 The transitions between the dressed states. The thicker dashed lines indicate that the population is larger in the $|-,\cdot\rangle$ states. 12

2.4 Ring cavity geometry and a probe beam (red). The distances between the mirrors are the same as in the experiment ($d =$ 4 cm, $2\sqrt{2}$ cm, and $2\sqrt{2}$ cm along the probe beam). $r., t.$ denotes the amplitude reflection and transmission coefficients. 15

2.5 Comparison between the empty cavity (blue curve) and a cavity with a weak gain medium (yellow curve). 20

3.1 Simplified schematic of the experiment. 27

3.2 New experimental design. 28

3.3 Three ^{39}K dispensers connected to a feedthrough. Only a small part of these thin rods is actually potassium. 29

3.4 ^{39}K ampoule and its bellows. Bending the bellows broke the glass seal. 31

3.5 Pressure (red squares) measured by the gauge connected to the turbo pump and temperature (upward-pointing green triangles, downward-pointing blue triangles, and purple diamonds) of three different parts of the new vacuum system plotted as a function of time. 32

3.6 The D_2 line of ^{39}K and the hyperfine structure [51]. The transitions and detuning frequencies used for laser cooling are shown by red lines. The push beam is weak (about 0.7 mW and 1 mm of diameter) and misses the MOT so it has no role in cooling. It is only used for bringing atoms from the 2D MOT to the 3D MOT. 34

3.7 Simplified schematic of the MOT laser system. The green arrows denote beat note offset locks (only the frequencies are shown). PDH: photodiode for Pound-Drever-Hall frequency stabilisation [55, 56], PMF: polarisation maintaining optical fibre patch cord and couplers, (DP)AOM: (double-pass) acousto-optical modulator [54], PBS: polarising beam splitter, and TA: tapered amplifier. 35

3.8 New TA design in the experiment. The amplifier chip was in the centre. There was a Peltier module for temperature control between the small copper and large aluminium blocks. A small piece of black paper on the output side was blocking a small amount of light back-reflected by lenses. 37

3.9 TA output power as a function of driving current for 15 mW of seed power. 38
3.10 Ratio of cooling to repump power after the TA. The bigger green peak is the cooling and the smaller one is the repump. The frequency scale was given by the RF frequency of the repump AOM. The FSR of the cavity was about 3 GHz. . . . 39
3.11 2D MOT (left) and 3D MOT coils (right). 40
3.12 Simulated gradient of the 3D MOT coils as a function of coil diameter and separation. The aim is 10 $\frac{\mathrm{G}}{\mathrm{cm}}$, which is indicated by the light green surface. The parameter combinations that result in a gradient above the light green surface are suitable for our MOT. 41
3.13 Measured magnetic field of the 3D MOT coils along the strong axis. The red dots are data and the green line is a fit. The slope is (69.8 ± 0.0075) $\frac{\mu\mathrm{T}}{\mathrm{cm}}$. The offset on the x axis was only an arbitrary point on the translation stage where measurements were possible and the displacement of the translation stage was measured. The geometric centre could not be determined accurately in that setup. The biggest source of error was stray magnetic field from the optical table and the environment, which was not characterised as this measurement was performed on a different optical table and not in the real experiment. 42
3.14 2D MOT recorded as the camera was facing the nearest viewport. The push beam was blocked. 44
3.15 3D MOT. 4×10^8 atoms. 44

4.1 The ring cavity with the piezo and two counterpropagating clockwise (CW) and counterclockwise (CCW) modes. 46

4.2 The upgraded ring cavity with some damping. The piece of Viton is inside the red circle. 48

4.3 Simplified schematic of the probe laser system. The 852-nm laser (dashed brown lines) gives a far-off-resonant beam, which, in this setup, is only used to lock the science cavity (not shown). DPAOM: double-pass acousto-optical modulator and PMF: polarisation maintaining optical fibre patch cord and couplers. The ^{39}K cell is set up for frequency-modulation spectroscopy [59]. 49

4.4 Upgrades to the cavity optics. PD: power detection (photodiodes or photon counters), and SMF: single-mode optical fibre patch cord. Long-pass and short-pass filters (not shown) were still used to block either of the two wavelengths. 51

4.5 Left: 3D MOT in the ring cavity. Right: the first step to move the MOT to the right place. The pictures were taken on different days with different camera settings, but can still illustrate what it is like to work with atoms and cavities at the same time. The MOT was roughly 10 times larger than the smallest cavity waist. 52

4.6 Bare atom energy levels and the atom-cavity system. The energy levels are split by twice the coupling constant g describing the interaction strength between the atom and the cavity mode. 53

4.7 Rabi splitting (yellow curve) for $\Omega = \frac{6\Gamma^2}{\omega_0}$ (arbitrary choice). The blue curve shows the empty cavity. The cavity-atom detuning is 0. 55

4.8 Rabi splitting for increasing atom number. Red: fits to the data. Blue: measurements. This picture was taken from [58]. 55

5.1 Left: 3D MOT under normal conditions. Right: 3D MOT distorted by the probe beam coming from the right side. This proves that we were probing the MOT. 59

5.2 Simplified schematic of the gain measurement. 59

5.3 Cavity transmission for calibration of the gain measurement. The green lines show individually fitted Lorentzians. The side peaks show the frequency modulation at 17.288 MHz. 60

5.4 Gain peak near the $2 \rightarrow 2'$ (cooling) transition. The frequencies are relative to the Stark shifted $2 \rightarrow 3'$ transition (see Figure 3.6 for D_2 energy levels) and the third nearby transition $2 \rightarrow 1'$ is not strong enough to be seen in this measurement. The vertical black line shows the cooling frequency given by the beat note between the cooling and probe beams. The data should follow the blue line outside the gain/absorption features, but there was too much noise during the ramp. . . . 61

5.5 Gain peak as a function of MOT cooling detuning. The dashed black line shows the theory curve (see Equation (2.7) and [43]). The pump (cooling) detuning is relative to the $2 \rightarrow 3'$ (strongest) transition. -27 MHz is the normal detuning optimised for the highest atom number, but the centre frequency of the gain peak does not depend on atom number and the gain peak is resolvable as long as the atom number is not too low. 63

5.6 Rescaled false-colour pictures of counterpropagating TEM_{00} and TEM_{11} lasing modes. Top peak: CCW. Bottom peak: CW. 66

5.7 Rescaled pictures of the counterpropagating lasing modes with increasing power (original ROI area = 4024.80 μm × 4411.80 μm). The power shown in each picture corresponds to the total optical power. 67

5.8 Beam profiler calibration based on Figure 5.7, knowing the total optical power for each picture. 68

5.9 Laser threshold curve as a function of the total atom number in the MOT. Red curves: CW. blue triangles: CCW. The solid black line is a fit with the slope of 2.8 fW/atom and the threshold atom number of 6.2×10^7. 70

5.10 Simplified schematic of the $g^{(2)}$ measurement. NDF: neutral density filter, BS: beam splitter, SMF: single-mode optical fibre patch cord and couplers, SPCM: single photon counting module. Black paper and tapes were used to eliminate the background light. 73

5.11 $g^{(2)}(\tau)$ data. Blue: $g^{(2)}(\tau)$ of fluorescence and red: $g^{(2)}(\tau)$ of lasing. 75
5.12 Cavity output spectrum around the TEM_{00} peaks in both directions. Red and dashed blue curves show CW and CCW directions, respectively. 77
5.13 Histogram of the difference between the position of the counterpropagating TEM_{00} peaks, in cavity length. 78
5.14 Simplified schematic of the cross-correlation measurement. NDF: neutral density filter, SMF: single-mode optical fibre patch cord and couplers, and SPCM: single photon counting module. 79
5.15 Competition between the two directions. Red: CCW and blue: CW. The counts were integrated over 60 μs intervals. . 80
5.16 Cross-correlation of the counterpropagating laser modes. . . . 80

6.1 Raman gain uses the same type of configuration as Mollow gain. [18] describes this Raman gain scheme in an operating ^{87}Rb MOT (similar level structure to ^{39}K). 85
6.2 This configuration provides lasing when a cavity is tuned to either of the two lasing fields. The pump fields are tuned close to the D_1 and D_2 hyperfine levels. This scheme was used in [69]. 86
6.3 The sign of dispersion can be flipped. As explained in Section 2.1.1, $\mathrm{Im}(\chi) < 0$ means positive gain. 88

A.1 Simplified schematic of the SBS experiment. DPAOM: double-pass acousto-optical modulator, BS: beam splitter, FRC: fibre ring cavity, PDH: Pound-Drever-Hall frequency stabilisation, and AM: amplitude modulation. 90

A.2 Simplified schematic of the evanescent coupler. 92

A.3 A cascade of thresholds was measured as a function of input power to the fibre ring cavity. 93

A.4 Advancement of the pump beam. The pulse was detected before (input) and after (output) the cavity. The peak of the pulse had already left the cavity before it even entered the cavity. 94

List of Tables

3.1 Upgrades to the old vacuum system. 27

4.1 Ring cavity parameters. 47

List of References

[1] E. J. Post, *Sagnac effect*, Rev. Mod. Phys. **39** (2), 475 (1967).

[2] W. Chow, J. Gea-Banacloche, L. Pedrotti, V. Sanders, W. Schleich and M. Scully, *The ring laser gyro*, Rev. Mod. Phys. **57** (1), 61 (1985).

[3] M. S. Shahriar, G. S. Pati, R. Tripathi, V. Gopal, M. Messall and K. Salit, *Ultrahigh enhancement in absolute and relative rotation sensing using fast and slow light*, Physical Review A **75** (5), 053807 (2007).

[4] P. Meystre and M. Sargent, *Elements of Quantum Optics*. Springer (2007).

[5] L. Hilico, C. Fabre and E. Giacobino, *Operation of a "cold-atom laser" in a magneto-optical trap*, (EPL) Europhysics Letters **18** (8), 685 (1992).

[6] J. Tabosa, G. Chen, Z. Hu, R. Lee and H. Kimble, *Nonlinear spectroscopy of cold atoms in a spontaneous-force optical trap*, Physical Review Letters **66** (25), 3245 (1991).

[7] D. Grison, B. Lounis, C. Salomon, J. Courtois and G. Grynberg, *Raman spectroscopy of cesium atoms in a laser trap*, EPL (Europhysics Letters) **15** (2), 149 (1991).

[8] M. Mitsunaga, T. Mukai, K. Watanabe and T. Mukai, *Dressed-atom spectroscopy of cold Cs atoms*, JOSA B **13** (12), 2696–2700 (1996).

[9] J. McKeever, A. Boca, A. D. Boozer, J. R. Buck and H. J. Kimble, *Experimental realization of a one-atom laser in the regime of strong coupling*, Nature **425** (6955), 268 (2003).

[10] J. Chen, *Active optical clock*, Chinese Science Bulletin **54** (3), 348–52 (2009).

[11] D. Meiser, J. Ye, D. R. Carlson and M. J. Holland, *Prospects for a millihertz-linewidth laser*, Physical Review Letters **102** (16), 163601 (2009).

[12] J. G. Bohnet, Z. Chen, J. M. Weiner, D. Meiser, M. J. Holland and J. K. Thompson, *A steady-state superradiant laser with less than one intracavity photon*, Nature **484** (7392), 78–81 (2012).

[13] M. A. Norcia, J. R. Cline, J. A. Muniz, J. M. Robinson, R. B. Hutson, A. Goban, G. E. Marti, J. Ye and J. K. Thompson, *Frequency measurements of superradiance from the strontium clock transition*, Physical Review X **8** (2), 021036 (2018).

[14] M. A. Norcia, M. N. Winchester, J. R. Cline and J. K. Thompson, *Superradiance on the millihertz linewidth strontium clock transition*, Science Advances **2** (10), e1601231 (2016).

[15] J. G. Bohnet, Z. Chen, J. M. Weiner, K. C. Cox and J. K. Thompson, *Active and passive sensing of collective atomic coherence in a superradiant laser*, Physical Review A **88** (1), 013826 (2013).

[16] J. M. Weiner, K. C. Cox, J. G. Bohnet, Z. Chen and J. K. Thompson,

Superradiant Raman laser magnetometer, Applied Physics Letters **101** (26), 261107 (2012).

[17] W. Guerin, F. Michaud and R. Kaiser, *Mechanisms for lasing with cold atoms as the gain medium*, Physical Review Letters **101** (9), 093002 (2008).

[18] G. Vrijsen, O. Hosten, J. Lee, S. Bernon and M. A. Kasevich, *Raman lasing with a cold atom gain medium in a high-finesse optical cavity*, Physical Review Letters **107** (6), 063904 (2011).

[19] R. Sawant and S. A. Rangwala, *Lasing by driven atoms-cavity system in collective strong coupling regime*, Scientific Reports **7** (1), 11432 (2017).

[20] H. Gothe, D. Sholokhov, A. Breunig, M. Steinel and J. Eschner, *Continuous-wave virtual-state lasing from cold ytterbium atoms*, Physical Review A **99** (1), 013415 (2019).

[21] A. Schilke, C. Zimmermann, P. W. Courteille and W. Guerin, *Optical parametric oscillation with distributed feedback in cold atoms*, Nature Photonics **6** (2), 101 (2012).

[22] D. Kruse, C. von Cube, C. Zimmermann and P. W. Courteille, *Observation of lasing mediated by collective atomic recoil*, Physical Review Letters **91** (18), 183601 (2003).

[23] Q. Baudouin, N. Mercadier, V. Guarrera, W. Guerin and R. Kaiser, *A cold-atom random laser*, Nature Physics **9** (6), 357 (2013).

[24] L. Mudarikwa, *Cold Atoms in a Ring Cavity.* Ph.D. thesis, University of Birmingham (2015).

[25] K. Pahwa, *Magneto Optical Trapping of Potassium-39 in a Ring Cavity*. Ph.D. thesis, University of Birmingham (2014).

[26] R. Culver, *Collective Strong Coupling of Cold Potassium Atoms in an Optical Ring Cavity*. Ph.D. thesis, University of Birmingham (2017).

[27] A. Lampis, *Coherent Light-Matter Interactions with Potassium Atoms*. Ph.D. thesis, University of Birmingham (2018).

[28] P. R. Berman and V. S. Malinovsky, *Principles of Laser Spectroscopy and Quantum Optics*. Princeton University Press (2011).

[29] A. E. Siegman, *Lasers*. University Science Books (1986).

[30] D. A. Steck, *Classical and Modern Optics*, (2013). `http://atomoptics-nas.uoregon.edu/~dsteck/teaching/optics/`.

[31] R. W. Boyd, *Nonlinear Optics*. Academic Press (2008).

[32] R. W. Boyd and D. J. Gauthier, *"Slow" and "fast" light*, Progress in Optics **43** 497–530 (2002).

[33] C. J. Foot, *Atomic Physics*. Oxford University Press (2005).

[34] R. W. Boyd, *Material slow light and structural slow light: similarities and differences for nonlinear optics [Invited]*, JOSA B **28** (12), A38–A44 (2011).

[35] B. R. Mollow, *Stimulated emission and absorption near resonance for driven systems*, Physical Review A **5** (5), 2217 (1972).

[36] F. Y. Wu, S. Ezekiel, M. Ducloy and B. R. Mollow, *Observation of Amplification in a Strongly Driven Two-Level Atomic System at Optical Frequencies*, Physical Review Letters **38** (19), 1077 (1977).

[37] J. Mompart and R. Corbalán, *Lasing without inversion*, J. Opt. B: Quantum Semiclass. Opt. **2** (3), R7 (2000).

[38] D. A. Steck, *Quantum and Atom Optics*, (2014). `http://atomoptics-nas.uoregon.edu/~dsteck/teaching/quantum-optics/`.

[39] H. M. Wiseman, *How many principles does it take to change a light bulb... into a laser?*, Physica Scripta **91** (3), 033001 (2016).

[40] I. D. Samuel, E. B. Namdas and G. A. Turnbull, *How to recognize lasing*, Nature Photonics **3** (10), 546 (2009).

[41] R. Loudon, *The Quantum Theory of Light*. OUP Oxford (2000).

[42] S. Barnett and P. M. Radmore, *Methods in Theoretical Quantum Optics*, vol. 15. Oxford University Press (2002).

[43] B. Megyeri, G. Harvie, A. Lampis and J. Goldwin, *Directional Bistability and Nonreciprocal Lasing with Cold Atoms in Ring Cavity*, Physical Review Letters **121** (16), 163603 (2018).

[44] G. Stedman, *Ring-laser tests of fundamental physics and geophysics*, Reports on Progress in Physics **60** (6), 615 (1997).

[45] N. V. Kravtsov and N. N. Kravtsov, *Nonreciprocal effects in ring lasers*, Quantum Electronics **29** (5), 378 (1999).

[46] A. Yariv and P. Yeh, *Photonics: Optical Electronics in Modern Communications*. Oxford University Press (2007).

[47] M. Sargent III, M. Scully and J. WE Lamb, *Laser Physics*. Addison-Wesley (1974).

[48] H. Yum and M. Shahriar, *Pump–probe model for the Kramers–Kronig relations in a laser*, Journal of Optics **12** (10), 104018 (2010).

[49] H. J. Metcalf and P. van der Straten, *Laser Cooling and Trapping*. Springer (1999).

[50] V. Letokhov, *Laser Control of Atoms and Molecules*. Oxford University Press (2007).

[51] T. Tiecke, *Properties of Potassium*, (2011). `http://www.tobiastiecke.nl/archive/PotassiumProperties.pdf`.

[52] K. Pahwa, L. Mudarikwa and J. Goldwin, *Polarization spectroscopy and magnetically-induced dichroism of the potassium D2 lines*, Opt. Express **20** (16), 17456–17466 (2012).

[53] *PID Theory Explained*. National Instruments (2011).

[54] E. Donley, T. Heavner, F. Levi, M. Tataw and S. Jefferts, *Double-pass acousto-optic modulator system*, Review of Scientific Instruments **76** (6), (2005).

[55] E. D. Black, *An introduction to Pound–Drever–Hall laser frequency stabilization*, American Journal of Physics **69** (1), 79–87 (2001).

[56] R. W. Fox, C. W. Oates and L. W. Hollberg, *Stabilizing diode lasers to high-finesse cavities*, Experimental Methods in the Physical Sciences **40** 1–46 (2003).

[57] R. S. W. III, *Magneto-optical trapping of potassium atoms*. Ph.D. thesis, University of Wisconsin-Madison (1997).

[58] R. Culver, A. Lampis, B. Megyeri, K. Pahwa, L. Mudarikwa, M. Holynski, P. Courteille and J. Goldwin, *Collective strong coupling*

of cold potassium atoms in a ring cavity, New Journal of Physics **18** (11), 113043 (2016).

[59] L. Mudarikwa, K. Pahwa and J. Goldwin, *Sub-Doppler modulation spectroscopy of potassium for laser stabilization*, Journal of Physics B: Atomic, Molecular and Optical Physics **45** (6), 065002 (2012).

[60] Y. Zhu, D. J. Gauthier, S. Morin, Q. Wu, H. Carmichael and T. Mossberg, *Vacuum Rabi Splitting as a feature of linear-dispersion theory: Analysis and experimental observations*, Physical Review Letters **64** (21), 2499 (1990).

[61] W. Nagourney, *Quantum Electronics for Atomic Physics and Telecommunication*. OUP Oxford (2014).

[62] B. E. Saleh and M. C. Teich, *Fundamentals of Photonics*. John Wiley & Sons (2019).

[63] R. H. Brown and R. Twiss, *A Test of a New Type of Stellar Interferometer on Sirius*, Nature **178** (4541), 1046–1048 (1956).

[64] M. Hennrich, A. Kuhn and G. Rempe, *Transition from antibunching to bunching in cavity QED*, Physical Review Letters **94** (5), 053604 (2005).

[65] E. Jakeman, C. Oliver and E. Pike, *The effects of spatial coherence on intensity fluctuation distributions of Gaussian light*, Journal of Physics A: General Physics **3** (5), L45 (1970).

[66] H. Carmichael, P. Drummond, P. Meystre and D. Walls, *Intensity correlations in resonance fluorescence with atomic number fluctuations*, Journal of Physics A: Mathematical and General **11** (5), L121 (1978).

[67] H. Kimble, M. Dagenais and L. Mandel, *Multiatom and transit-time effects on photon-correlation measurements in resonance fluorescence*, Physical Review A **18** (1), 201 (1978).

[68] N. B. Phillips, I. Novikova, E. E. Mikhailov, D. Budker and S. Rochester, *Controllable steep dispersion with gain in a four-level N-scheme with four-wave mixing*, Journal of Modern Optics **60** (1), 64–72 (2013).

[69] D. T. Kutzke, O. Wolfe, S. M. Rochester, D. Budker, I. Novikova and E. E. Mikhailov, *Tailorable dispersion in a four-wave mixing laser*, Optics Letters **42** (14), 2846–2849 (2017).

[70] A. Wicht, K. Danzmann, M. Fleischhauer, M. Scully, G. Müller and R.-H. Rinkleff, *White-light cavities, atomic phase coherence, and gravitational wave detectors*, Optics Communications **134** (1), 431–439 (1997).

[71] J. Yablon, Z. Zhou, N. Condon, D. Hileman, S. Tseng and S. Shahriar, *Demonstration of a highly subluminal laser with suppression of cavity length sensitivity by nearly three orders of magnitude*, Optics Express **25** (24), 30327–30335 (2017).

[72] G. Pati, M. Salit, K. Salit and M. Shahriar, *Demonstration of a tunable-bandwidth white-light interferometer using anomalous dispersion in atomic vapor*, Physical Review Letters **99** (13), 133601 (2007).

[73] L. F. Stokes, M. Chodorow and H. J. Shaw, *All-single-mode fiber resonator*, Optics Letters **7** (6), 288–290 (1982).